Energy Production, Frictional Dissipation, and Maximum Intensity of a Numerically Simulated Tropical Cyclone

Yuqing Wang[1] and Jing Xu

International Pacific Research Center and Department of Meteorology

University of Hawaii at Manoa, Honolulu, HI 96822

May 19, 2009

Dateline

Revised for ***Journal of the Atmospheric Sciences***

---

[1]Corresponding author: Dr. Yuqing Wang, IPRC/SOEST, University of Hawaii at Manoa, 1680 East-West Road, Honolulu, HI 96822, Email: yuqing@hawaii.edu

Abstract

A tropical cyclone (TC) viewed as a heat engine converts heat energy extracted from the ocean to kinetic energy of the TC, which is eventually dissipated due to surface friction. Since the energy production rate is a linear function while the frictional dissipation rate is a cubic power of surface wind speed, the dissipation rate is generally smaller than the production rate initially but increases faster than the production rate as the storm intensifies. When the dissipation rate eventually reaches the production rate, the TC has no excess energy to intensify. Emanuel hypothesized that a TC achieves its maximum potential intensity (E-MPI) when the surface frictional dissipation rate balances the energy production rate near the radius of maximum wind (RMW).

Although the E-MPI agrees well with the maximum intensity of numerically simulated TCs in earlier axisymmetric models, the balance hypothesis near the RMW has not been evaluated. This study shows that the frictional dissipation rate in a numerically simulated mature TC is about 25% larger than the energy production rate near the RMW, while the dissipation rate is lower than the energy production rate outside the eyewall. This finding implies that the excess frictional dissipation under the eyewall should be partially balanced by the energy production outside the eyewall and thus the local balance hypothesis underestimates the TC maximum intensity. Both Lagrangian and control volume equivalent potential temperature (θ_e) budget analyses demonstrate that the energy gained by boundary layer inflow air due to surface entropy fluxes outside and prior to interaction with the eyewall contributes significantly to the energy balance in the eyewall through the lateral inward energy flux. This contribution is further verified using a sensitivity experiment in which the surface entropy fluxes are eliminated outside a radius of 30-45 km, which leads to a 13.5% reduction of the maximum sustained near-surface wind and a largely reduced size of the model TC.

1. Introduction

Tropical cyclones (TCs) form over the tropical oceans with sea surface temperature (SST) higher than 26°C and an isothermal layer extending from the surface to a depth about 60 m (Gray 1975; Malkus and Riehl 1960). Both a deep oceanic mixed layer and a threshold SST are necessary to assure sufficient energy supply from the underlying ocean for the development and maintenance of a TC, which is often viewed as a heat/Carnot engine (Emanuel 1986, 1988, 1991, 1995, 1997).

In his theory of TC maximum potential intensity (MPI), Emanuel (1995, 1997) assumed that at steady state, namely when the storm reached its MPI, the rate of entropy production from the ocean should be approximately balanced by the surface frictional/mechanical dissipation to the ocean, namely,

$$\int_{r_m}^{r_o} \rho \varepsilon T_s C_k \left|\vec{V}\right| (s_0^* - s_b) r dr = \int_{r_m}^{r_0} \rho C_D \left|\vec{V}\right|^3 r dr \,, \qquad (1)$$

where r is the radius, r_m is the radius of the eyewall and roughly the radius of maximum wind (RMW), r_0 is an outer radius far away from the RMW, ρ is the air density of the subcloud layer, T_s is SST, $\left|\vec{V}\right|$ is the near surface wind speed, s_0^* is the saturation entropy of the ocean surface, s_b is the entropy of subcloud-layer air, C_k is the exchange coefficient of entropy flux from the ocean, C_D is the surface drag coefficient, and ε is the thermodynamic efficiency of the heat engine, which is defined as

$$\varepsilon = \frac{T_s - T_0}{T_s} \,, \qquad (2)$$

where T_0 is the outflow layer air temperature. Note that (2) is expressed in a form that does not

take into account the dissipative heating in the boundary layer, otherwise the denominator T_s should be replaced by T_0 (Bister and Emanuel 1998). Emanuel (1997) assumed that the largest contributions to both integrals in (1) come from the flow near the RMW and therefore the balance in (1) could be evaluated near the RMW in the boundary layer. This leads to an expression for the maximum wind speed, namely the MPI

$$\left|\vec{V}_m\right| \approx \sqrt{\frac{C_k}{C_D}\varepsilon T_s (s_0^* - s_b)}\Big|_{r_m}, \qquad (3)$$

where $\left|\vec{V}_m\right|$ is the maximum wind speed, the subscript "m" indicates that the value is evaluated near the RMW. Emanuel (1997) indicated that although (3) was derived as an approximation, it has the same form as an expression, which was derived analytically from the entropy balance of the subcloud layer in the eyewall with the assumption that entropy is constant along angular momentum surfaces (Emanuel 1986, 1995, 1997, hereafter denoted E-MPI). Thus, the maximum wind speed in (3) can be calculated by specifying a value of relative humidity of the subcloud layer outside of r_m SST, and the ratio of exchange and drag coefficients.

Although earlier numerical results from axisymmetric TC models demonstrated that the E-MPI can give an excellent estimation of the model TC maximum intensity (Rotunno and Emanuel 1987; Emanuel 1995, 1997), recent studies show that numerically simulated TC maximum intensity can exceed the E-MPI when very high-resolution models are used (Persing and Montgomery 2003, 2005; Cram et al. 2007; Yang et al. 2008; Bryan and Rotunno 2009a). These high-resolution model results are supported by recent observational studies (Montgomery et al. 2006; Bell and Montgomery 2008). In fact, the intensities of both modeled and observed

TCs can be considerably higher than the E-MPI by as much as 10-50% (Persing and Montgomery 2003, 2005; Yang et al. 2008; Bryan and Rotunno 2009a; Montgomery et al. 2006). Such a phenomenon was termed superintensity by Persing and Montgomery (2003, hereafter PM03). They hypothesized that the near-surface high entropy air in the eye region could serve as an additional source of energy for the TC heat engine if the air is transported into the eyewall and thus considerably increase the TC intensity (Cram et al. 2007). This possible effect has not been included in the E-MPI theory.

This high-entropy anomaly hypothesis of PM03 was tested recently by Bryan and Rotunno (2009a, hereinafter BR09) using a very high-resolution axisymmetric TC model. They set the surface entropy fluxes to be zero in the eye so that the local high-entropy anomaly near the surface in the eye was eliminated. Removal of the high entropy anomaly in the eye only resulted in a slightly weaker storm as evidenced by the maximum tangential wind speed (reduced by about 4% on average). This reduction in maximum wind speed is far too small to explain the more than 50% higher maximum intensity obtained in their simulation compared with that estimated by the E-MPI theory. BR09 found that less than 3% of the total surface entropy input to the TC could be attributed to air from the eye because of the relatively small volume of the eye and thus the total magnitude of entropy transport from the eye to the eyewall was negligible in the entropy budget of the simulated TC. Since BR09 used an axisymmetric model, they might have underestimated the lateral mixing between the eye and the eyewall due to the existence of strong eddies and vortex Rossby waves across the eyewall region (e.g., Wang 2002a, b; Yang et

al. 2008). However, this seems unlikely to be a major factor since the eye volume is quite small compared with the eyewall volume as BR09 indicated.

Smith et al. (2008) showed that the assumption of gradient wind balance in the boundary layer is a major shortcoming of the E-MPI theory and is responsible for the systematic underestimation of TC intensity. They suggested the use of a more complete dynamic boundary layer model in E-MPI. In a recent study, Bryan and Rotunno (2009c) presented a more complete analytic model and demonstrated that the unbalanced flow in the boundary layer could contribute significantly to TC maximum intensity. These two studies focused on the deficiency in the dynamical aspect of the E-MPI. From the energy balance point of view, expression (1) does not include any approximation for the boundary layer flow. Therefore, it still remains a major issue in the viewpoint of energetics why the E-MPI considerably underestimates the actual TC maximum intensity from both numerical models and observations.

In addition to uncertainty in the possible contribution from the eye region, the E-MPI defined in (3) is determined without any explicit contributions of energy production outside the eyewall. Although the approximation (3) has the same form as the solution derived analytically (Emanuel 1986, 1995, 1997), we could expect that both the approximation for (3) and the assumptions used to derive the exact solution might deviate considerably from the original energy balance given in (1). Motivated by this hypothesis, we attempt to evaluate the validity of (3) as an approximation to (1) in this study and to understand why the E-MPI considerably underestimates the maximum intensity of TCs in numerical simulations and observations. We

will demonstrate that the discrepancy between the maximum intensities in the simulation and estimated by the E-MPI can be easily explained by the deviation of the approximation (3) from the original energy balance equation (1). We will show how surface entropy fluxes outside the eyewall contribute to the energy budget in the eyewall and thus the maximum intensity of a TC.

The rest of the paper is organized as follows. Section 2 describes the numerical model and the experimental design. An overview of the simulated TC and the corresponding theoretical E-MPI are given in section 3. Section 4 evaluates the validity of the approximation (3) to the original energy balance equation (1) in a control simulation. The discrepancies are interpreted in section 5 based on both Lagrangian and control volume equivalent potential temperature budget analyses and a sensitivity experiment. Some related issues are discussed in section 6. The main conclusions are drawn in the last section.

2. Model and experimental design

The model used in this study is the fully compressible, nonhydrostatic, primitive equation model–TCM4 developed by Wang (2007). TCM4 has been used recently to study the inner-core dynamics of TCs (Wang 2008a, b, 2009). A full description of TCM4 can be found in Wang (2007). The model settings in this study are the same as those used in Wang (2008a, b, 2009). The model uses a mass coordinate in the vertical dimension with the lower boundary at the flat surface with the unperturbed surface pressure of 1010 hPa and with its top at about 38 km. The model domain is quadruply nested with two-way interactive nesting and with the inner meshes automatically movable to follow the model TC as in TCM3 (Wang 2001, 2002c). The model has 26 vertical levels with relatively high resolution both in the lower troposphere and near the

tropopause. The horizontal grid sizes of 67.5, 22.5, 7.5, and 2.5 km have domain dimensions of 251×151, 109×109, 127×127, and 163×163 grid points for the four meshes, respectively.

The model physics include an E-ε turbulence closure scheme for subgrid scale vertical turbulent mixing (Langland and Liou 1996); a modified Monin-Obukhov scheme for the surface flux calculations (Fairall et al. 2003); an explicit treatment of the mixed-phase cloud microphysics (Wang 2001); a nonlinear fourth-order horizontal diffusion for all prognostic variables except for that related to the mass conservation equation; a simple Newtonian cooling term, which is added to the perturbation potential temperature equation to mimic the radiative cooling in the model (Rotunno and Emanuel 1987); and the dissipative heating due to molecular friction related to the turbulent kinetic energy dissipation rate (ε_e) from the E-ε turbulent closure scheme. As in Wang (2007, 2008a, b, 2009), the same model physics are used in all meshes. Since no large-scale environmental flow is included in this study, convection is mainly active in both the inner-core region and spiral rainbands that occur mainly within about 200 km from the TC center and thus are covered by the finest innermost domain. Therefore, cumulus parameterization is not considered even in the two outermost meshes in this study.

The experimental design follows Wang (2008a, b, 2009). The model was initialized with an axisymmetric cyclonic vortex on an f–plane of 18°N in a quiescent environment over the ocean with a constant SST of 29°C. The initial thermodynamic structure of the unperturbed model atmosphere is defined as the western Pacific clear-sky environment given by Gray et al. (1975). The initial cyclonic vortex has a maximum tangential wind speed at the surface of 20 m s^{-1} at a radius of 80 km that decreases sinusoidally with normalized pressure to vanish at 100 hPa and radially outward exponentially (Wang 2007). The mass and thermodynamic fields are obtained by solving the nonlinear balance equation as described in Wang (2001). The simulation was for 240 h

with all standard model settings (namely control experiment). In addition, a sensitivity experiment was conducted, which will be detailed in section 5.

3. An overview of the simulated TC

Figure 1 shows the evolution of the maximum azimuthal mean wind speed at the lowest model level (about 35 m from the sea surface) and the minimum central sea level pressure of the simulated TC in the control experiment. The TC experienced its rapid intensification in the first 72 h after an initial adjustment. This was followed by a slow intensification until the storm reached its maximum intensity with the maximum azimuthal mean wind speed of about 68.2 m s^{-1} and a minimum central sea level pressure of around 913.5 hPa averaged between 144-192 h of simulation. The storm maintained its maximum intensity for about 3 days before it weakened slowly for a short period due to the formation of an annular hurricane structure (Wang 2008b).

Figure 2 shows the axisymmetric structure of the model TC after 168 h of simulation in the control experiment. The storm has its maximum tangential wind over 80 m s^{-1} in the lowest 1 km layer at a radius of about 17.5 km (Fig. 2a), a shallow inflow layer in the lowest atmospheric boundary layer and a relatively deep outflow layer in the upper troposphere (Fig. 2b). The eyewall ascent tilts radially outward with height, especially above 5-km altitude (Fig. 2c). The storm has a warm-core structure through the depth of the troposphere with the maximum temperature anomaly over 16^{o}C in the eye region in the upper troposphere (Fig. 2d). There are some negative temperature anomalies under and outside the eyewall mainly due to the evaporation of rain water.

The storm shows an off-centered potential vorticity (PV) maximum just inside the RMW through the depth of the troposphere (Fig. 2e). This PV structure satisfies the necessary condition for barotropic instability and thus is dynamically unstable to small perturbations, favoring the formation of asymmetric eddies characterized by vortex Rossby waves in the eyewall (e.g., Wang 2001, 2002a, b). The asymmetric structure of the simulated TC in the control experiment can be found in Wang (2008b). Equivalent potential temperature (θ_e) is high in the eye and eyewall with local maxima near the surface in the eye and in the upper troposphere (Fig. 2f). Relatively high θ_e also appears in the inflow boundary layer and increases gradually toward the eyewall near the surface, an indication of the inflow boundary layer air acquiring energy from the underlying ocean as the air spirals cyclonically inward to the eyewall (see further discussion in section 5).

The RMW in the control experiment decreased rapidly with time in the first 20 h and reached its minimum of 15 km by 48 h of simulation (Fig. 3) as the storm experienced the rapid intensification (Fig. 1). An increase in the RMW occurred after 192 h of simulation, which was associated with the transition of the model storm from a regular hurricane structure to an annular hurricane structure identified from observations by Knaff et al. (2003). Specifically, the storm was characterized by a large eye, large outward slope of the wide eyewall ascent, and the lack of active outer spiral rainbands after the transition (see Wang 2008b for details). Accompanied by the transition was a slight weakening of the storm intensity (Fig. 1) and an increase of the inner core size of the storm (Fig. 3).

A comparison of the simulated storm intensity with the theoretical E-MPI would be

helpful for the discussion in the following sections. The E-MPI is a function of the ratio of the exchange coefficient to the drag coefficient (C_k/C_D), the given SST and the atmospheric thermodynamic structure, and the subcloud layer relative humidity (RH) in the environment (Bister and Emanuel 2002). With the initial atmospheric sounding and the constant SST used in the model simulation in this study, the E-MPI can then be calculated with a given environmental RH in the inflow boundary layer and the ratio C_k/C_D. RH in the boundary layer is about 85% in the initial model atmospheric sounding. The ratio C_k/C_D in the E-MPI calculation is given 0.8 as a recommended value (Emanuel 1995, 1997; Bister and Emanuel 2002). However, in our model simulation, the ratio C_k/C_D is a function of wind speed and thus a function of radius (Fig. 4). It is as small as 0.32 near the RMW and is about 0.4 averaged in the area within a radius of about 50 km from the storm center. Calculation of the E-MPI also depends on the assumption for the eyewall ascent, namely assuming either a reversible or a pseudo-adiabatic process. The assumption of the pseudo-adiabatic eyewall ascent results in an E-MPI of about 8-10% higher in terms of the maximum near surface wind speed and a lower outflow layer temperature than the assumption of the reversible ascent for the same SST and environmental conditions (Table 1).

With 0.8 for C_k/C_D, the reversible assumption results in an MPI very close to the storm intensity in the control simulation but the pseudo-adiabatic assumption leads to an MPI about 7% stronger in the maximum near-surface wind speed than that of the simulated storm (Table 1). However, the ratio C_k/C_D in the model is larger than 0.8 only near the storm center because of the light winds and is generally smaller than 0.5 within a radius of 70 km (Fig. 4). Since the E-PMI

theory assumes a balance between the energy production and dissipation near the RMW (Emanuel 1995, 1997), the value of C_k/C_D near the RMW (0.32) should be used in the E-MPI calculation for a fair comparison with the model TC intensity. This leads to 41.5 m s^{-1} and 45.5 m s^{-1} in the maximum near surface wind speed for the reversible and pseudo-adiabatic E-MPIs, respectively, which are about 39% and 33% weaker than the TC intensity in the control simulation. If an area-averaged ratio within a radius of 50 km (0.4) is used, higher reversible and pseudo-adiabatic E-MPIs can be obtained (46.7 m s^{-1} and 51.1 m s^{-1}, respectively) but they are still about 30% and 25% smaller than the maximum wind speed of the model storm. Therefore, consistent with previous findings (Persing and Montgomery 2003; Yang et al. 2008; BR09), the E-MPI considerably underestimates the maximum intensity of the simulated storm in the control experiment. Note that it is not our intent to justify whether the small ratio of C_k/C_D in the model is reasonable. Rather, we attempt to evaluate the validity of the balance assumption used in the theoretical derivation of the E-MPI based on the simulated storm in the model.

4. Energy production and dissipation in the simulated TC

To evaluate the energy production and frictional dissipation rates in the simulated TC, we calculated both the total and individual components of energy production rate from the model output. In (1), Emanuel (1997) only considered the surface entropy flux as the energy production rate, while both dissipative heating and Newtonian cooling were included in our model simulation. As a result, the total energy production rate (PRODUCTION) and the frictional dissipation rate (DISSIPATION) in the model can be written as follows, respectively

$$PRODUCTION = 2\pi \int_0^{r_0} P_D r dr \,, \tag{4}$$

$$DISSIPATION = 2\pi \int_0^{r_0} D_S r dr \,, \tag{5}$$

where

$$P_D = \varepsilon(SH + LH + DHT + RAD) \,, \tag{6}$$

$$D_S = \frac{1}{2\pi} \int_0^{2\pi} \rho C_D \left|\vec{V}\right|^3 d\lambda \,, \tag{7}$$

And

$$SH = \frac{1}{2\pi} \int_0^{2\pi} \rho C_p C_k \left|\vec{V}\right| (T_s - T_a) d\lambda \,, \tag{8}$$

$$LH = \frac{1}{2\pi} \int_0^{2\pi} \rho L_v C_k \left|\vec{V}\right| (q_s - q_a) d\lambda \,, \tag{9}$$

$$DHT = \frac{1}{2\pi} \int_0^{2\pi} \left(\int_0^{H} \rho C_p D_H dz \right) d\lambda \,, \tag{10}$$

$$RAD = \frac{1}{2\pi} \int_0^{2\pi} \left(\int_0^{H} \rho C_p R_H dz \right) d\lambda \,, \tag{11}$$

where P_D and D_S are the azimuthal mean energy production and frictional dissipation rates; *SH*, *LH*, *DHT*, and *RAD* are, respectively, the azimuthal mean sensible heat flux, latent heat flux, column-integrated dissipative heating rate, and column-integrated radiative heating/cooling rate, λ is the azimuth, z is the height, H is the depth of the troposphere, C_p is the specific heat of dry air at constant pressure, L_v is the latent heat of vaporization, q_s is the saturation mixing ratio of water vapor at SST (T_s), T_a and q_a are the air temperature and water vapor mixing ratio at the lowest model level, C_k and C_D are evaluated at the lowest model level as well for consistency, D_H is the dissipative heating rate at a given grid point, and R_H is the Newtonian cooling rate as used in Rotunno and Emanuel (1987), namely

$$\frac{\partial T}{\partial t} = R_H = \left(\frac{p}{p_0} \right)^{R/C_p} \frac{(\theta_{ref} - \theta)}{\tau}, \qquad (12)$$

Here R is gas constant for dry air, p is pressure, p_0=1000 hPa is the reference pressure, T is temperature, θ is potential temperature, θ_{ref} is potential temperature of the unperturbed initial model atmosphere, and τ is the relaxation time which is set to be 12 h in the model. In order to avoid unrealistic radiative cooling rate in the warm core, the absolute value of R_H in (12) is not allowed to be larger than 2K d^{-1}. Note that the integrations in (6) and (7) are from $r = 0$ instead of from $r = r_m$ in (1) given by Emanuel (1997). This should not make any significant difference because the energy production and dissipation rates in the eye are quite small due to light winds and small volume (BR09).

For the sake of a direct comparison, the thermodynamic efficiency defined in (2) has been included in the energy production rate P_D, which can thus be referred to as the effective energy production available for kinetic energy production of the TC system. The thermodynamic efficiency is a function of the outflow layer temperature (2), which is weakly dependent on the storm intensity and the assumption for the eyewall ascent (Table 1). For the storm intensity in the control experiment, we can take the thermodynamic efficiency as 35.1%, which corresponds to T_s of 302.15 K and T_0 of 196.1 K for the reversible E-MPI. Note that it is not our purpose to conduct a closed energy budget in this section. Instead, we evaluate the evolution of the energy production rate, the frictional dissipation rate, and the corresponding intensity change of the simulated TC. In particular, we will examine the validity of (3) as an approximation to (1) used by Emanuel (1997). Therefore we focus primarily on the radial distributions of the azimuthal

mean energy production and dissipation rates, namely P_D and D_S.

Because the energy production rate is a linear function of surface wind speed while the frictional dissipation rate is a cubic power of surface wind speed, P_D is much larger than D_S in the developing stage (Fig. 5a). As the storm intensifies, the frictional dissipation rate grows much faster than the energy production rate and D_S equals P_D under the eyewall after about 60 h of simulation (Fig. 5b). According to Emanuel (1997), this should roughly be the time that the storm reaches its maximum intensity. At this time, the storm has the maximum azimuthal mean wind speed of 61.4 m s^{-1} at the lowest model level and a minimum central sea level pressure of 942 hPa. However, this is only about 90% of the 144-192 h averaged maximum intensity of the model TC in terms of the azimuthal mean wind speed and about 28.5 hPa higher in the central sea level pressure than the 144-192 h average. After this point, the storm continues to intensify but with a much slower intensification rate (Fig. 1). Meanwhile, the frictional dissipation rate grows faster, exceeding the energy production rate under the eyewall (Figs. 5c, 5d, and 6). For example, D_S is about 11% and 25% larger than P_D near the RMW, respectively, at 72 h (Fig. 5c) and averaged between 144 h and 192 h of simulation (Fig. 5d) during which time the model storm reaches its maximum intensity (Fig. 1).

The above results demonstrate that the use of (3) as an approximation to (1) in Emanuel (1997) would lead to considerable underestimation of the maximum intensity since the energy production rate could not approximately balance the frictional dissipation rate near the RMW in the mature stage (Fig. 6). Emanuel (1997) assumed that contributions outside the eyewall to the

integrals on both sides in (1) are negligible compared to those from the flow near the RMW. This is true for the frictional dissipation rate but not for the energy production rate in our simulation (Fig. 5). Note that P_D is generally larger than D_S outside the eyewall (namely beyond a radius of about 30 km in our simulation). Because of the large area coverage outside the eyewall, the energy production rate outside the eyewall should contribute significantly to the radial integral in (4) and also the left hand side in (1). Therefore from the viewpoint of the energy gain and loss, there should be a net energy transport from outside of the eyewall region to the eyewall in a TC (see further discussion in section 5). This indicates that the local balance between the energy production and frictional dissipation rates near the RMW for the storm maximum intensity would underestimate the actual maximum intensity of the storm. This finding is consistent with the recent results of BR09, who found that surface entropy fluxes outside the eyewall are important for TC intensity. They showed that even with the surface entropy fluxes under the eyewall eliminated, they still got a quite strong TC in their axisymmetric model (see their Fig. 5).

Figure 7 shows the different components of the energy production rate at given times and the time mean as given in Fig. 5. The surface latent heat flux is the major contributor to the energy production in the simulated TC at any given radius throughout the simulation, indicating that surface latent heat from the ocean is the major energy source of the TC engine. The surface sensible heat flux is about 15-25% of the surface latent heat flux within a radius of about 50 km and about 8-12% further outward. Dissipative heating is quite small when the storm is weak (Fig. 7a) but increases as the storm intensifies (Fig. 7b). Similar to the frictional dissipation rate (Fig.

5), dissipative heating rate is large only under the eyewall near the RMW (Fig. 7). During the period of the maximum intensity, contribution by dissipative heating is even larger than 1/3 of that by surface latent heat flux near the RMW (Fig. 7d). Radiative cooling contributes negatively to the energy production in the model. Its magnitude is about 6-10% of the surface latent heat flux near the RMW and is generally less than 30% of the surface latent heat flux within a radius of about 150 km. Although it was included in the numerical models in Emanuel (1995, 1997), the Newtonian cooling seemed to be ignored in his evaluation of the energy production rate. This could result in an overestimation of the energy production rate and thus the MPI in his comparison with numerical model results (see further discussion in section 6).

Since the energy production rate near the RMW could not balance the frictional dissipation rate, a natural question arises as to how far from the storm center, specifically within what outer radius r_0, can the balance between the integrated energy production and frictional dissipation rates given in (1) be reached. To address this question, we examined the area-integrated energy production and surface frictional dissipation rates as a function of r_0 in the control experiment (Fig. 8). Both the energy production and frictional dissipation rates integrated in the eye region are quite small, indicating that the contribution by surface entropy fluxes in the eye region to the energy budget of the TC system and thus the maximum intensity of the simulated storm is negligible, in agreement with BR09 but in contrast to the hypothesis of PM03. The area-integrated energy production and frictional dissipation rates become equal within a radius of 37.5 km in the control experiment (Fig. 8). Further outward the energy production rate

becomes larger than the frictional dissipation rate, indicating that the balance assumption should not be too far from the RMW, namely r_0 in (1) should be in the range of 2-2.5 times the RMW. We will show in the next section that inward transport of energy due to surface entropy fluxes within about 2-2.5 times the RMW is critical to the energy budget in the eyewall and thus the maximum intensity of the simulated storm in the control experiment. Although the actual value for r_0 may vary with model settings, such as the model resolution, the initial conditions, and so on, our results demonstrate that energy production outside the eyewall is needed to balance the frictional dissipation under the eyewall.

5. Interpretation

To understand how the energy production outside the eyewall is transported to the eyewall and contributes to the TC maximum intensity, we performed both Lagrangian and control volume θ_e budget analyses. A sensitivity experiment was also conducted to further verify the budget analyses in a fully interactive model TC system. With these budgets and the sensitivity experiment, the results discussed in the last section can be interpreted satisfactorily and understood easily.

a. A Lagrangian θ_e budget

The thermodynamic equation and water vapor conservation equation in TCM4 are

$$\frac{d\theta}{dt} = \frac{Q_{cond} + D_H + R_H}{C_p \Pi} + D_\theta + F_\theta , \tag{13}$$

$$\frac{dq_v}{dt} = -\frac{Q_{cond}}{L_v} + D_{qv} + F_{qv} , \tag{14}$$

where Q_{cond} is the condensational heating rate, D_θ and F_θ are changes in θ due to horizontal diffusion and vertical mixing, q_v is mixing ratio of water vapor, D_{qv} and F_{qv} are changes in q_v due to horizontal diffusion and vertical mixing, and $\prod = (p/p_0)^{R/Cp}$ with p the pressure and p_0 (=1000 hPa) the reference pressure. Note that the vertical mixing terms F_θ and F_{qv} include the effects of surface sensible and latent heat fluxes, respectively. Since θ_e is not a prognostic variable in the model, its change is approximated in the budget by (Rotunno and Emanuel 1987)

$$\frac{d\theta_e}{dt} \approx \frac{d\theta}{dt} + \frac{L}{C_p \Pi}\frac{dq_v}{dt} = D_{\theta e_e} + F_{\theta e} + \frac{1}{C_p \Pi}(D_H + R_H), \qquad (15)$$

where

$$D_{\theta e} = D_{\theta_e} + \frac{L}{C_p \Pi} D_{qv}, \quad F_{\theta e} = F_\theta + \frac{L}{C_p \Pi} F_{qv}, \qquad (16)$$

can be considered as changes in θ_e due to horizontal diffusion and vertical mixing with the latter including the surface entropy flux. For consistency, θ_e is estimated by $\theta_e \approx \theta + \frac{Lq_v}{C_p \Pi}$ in our budget analyses.

We define the vertical averaging as

$$\overline{(\ )} = \frac{1}{H}\int_0^H (\ ) dz, \qquad (17)$$

where H is the depth to which the vertical averaging is applied. Since our interest is to examine the change of θ_e for an air parcel along its trajectory cyclonically spiraling inward following the boundary layer inflow during the mature stage of the simulated storm, we choose H =212 m and calculated a Lagrangian budget for the steady-state storm in the control experiment, averaged between 144 h and 192 h of simulation. Figure 9 shows the spatial distribution of the time-mean

θ_e and horizontal winds averaged in the lowest 212 m for such a steady-state storm.

Since a steady flow is assumed and the vertical motion can be ignored outside the eyewall in the surface layer (Fig. 2c), we can simply estimate the equation for the θ_e change of an air parcel along its horizontal trajectory following the mean boundary layer flow by

$$\left.\frac{d\overline{\theta_e}}{dt}\right|_L \approx \overline{D_{\theta e}} + \overline{F_{\theta e}} + \overline{\frac{1}{C_p \Pi}\left(D_H + R_H\right)}, \qquad (18)$$

The terms on the right hand side are all time averaged between 144 h and 192 h of simulation. The terms were interpolated to the trajectory using cubic spine interpolation. We calculated different forward trajectories for parcels starting from different locations outside the eyewall and performed the Lagrangian $\overline{\theta}_e$ budget analysis using (18) with a forward-backward time integration scheme. Figure 9 shows one such trajectory for a parcel initially located 100 km east of the storm center. The parcel spirals cyclonically inward and reaches the RMW in about one and a half hours and then rotates cyclonically in the eyewall without significant radial movement. The orbital nature of the trajectory about the eyewall is not realistic at this altitude level since the air parcel should be lifted upward along the eyewall updraft; however, this effect is not considered in our simple budget analysis. Therefore interpretation of the $\overline{\theta}_e$ change after the air parcel enters the eyewall should be with caution. We further assume that at the starting point of each trajectory, the air parcel $\overline{\theta}_e$ is the same as its surroundings $\overline{\theta}_e$ at the same location.

Figure 10 shows the changes of $\overline{\theta}_e$ with time for an air parcel moving along the trajectory given in Fig. 9 in two calculations: in one calculation (EPT_SFLX), all source terms in (18) are included in the Lagrangian integration; whereas in the other calculation (EPT_NoSFLX)

the vertical mixing term including the surface entropy flux ($F_{\theta e}$) in (18) is ignored. Both the radial distance of the air parcel from its starting location and the local $\overline{\theta}_e$ (EPT_Model) at the point the air parcel arrives at the given time are also shown in Fig. 10. The air parcel with all source terms has $\overline{\theta}_e$ very similar to the local $\overline{\theta}_e$ before the air parcel enters the eyewall region (roughly within a radius of about 30 km in our simulation), but about 1 to 2 K lower than the local $\overline{\theta}_e$ after it moves within the eyewall region. This indicates that the horizontal Lagrangian θ_e budget we performed is accurate outside the eyewall where no significant vertical motion occurs. The lower $\overline{\theta}_e$ of the air parcel compared with the local $\overline{\theta}_e$ in the eyewall region could be due to some unrealistic assumptions in our Lagrangian budget equation (15), such as the steady state flow which assumes no vertical motion or vertical mixing with its surroundings. Nevertheless, this is not a serious problem here since we are mainly interested in how the surface fluxes outside the eyewall region affect the θ_e change just before the air parcel enters the eyewall region.

As we can see from Fig. 10, when the vertical mixing and the surface flux outside the eyewall region are excluded in the Langrangian θ_e budget (EPT_No_SFLX), the air parcel $\overline{\theta}_e$ is about 1.3 K lower than that in the budget calculated with the full source terms in EPT_SFLX. Although this is relatively small compared to the $\overline{\theta}_e$ in the eye and the eyewall, it would have a significant effect on the θ_e budget in the eyewall because the inflow air volume outside the eyewall is quite large compared to the volume of the eyewall (see discussion in section 5b). This is in sharp contrast to the high θ_e in the eye, but with relatively small total volume (BR09).

Therefore, if the energy production due to the surface entropy fluxes is ignored outside the eyewall region, the air in the boundary layer inflow entering the eyewall region would have a lower θ_e and thus be less energetic. This demonstrates that air parcels in the surface layer can extract non-negligible energy from the underlying ocean as they spiral cyclonically inward toward the eyewall region following the boundary layer inflow.

The increase in the boundary layer $\overline{\theta}_e$ due to surface entropy fluxes for an air parcel entering the eyewall depends on the time the air parcel travels to reach the eyewall region or alternatively on the initial radial distance of the air parcel (and also the radial distribution of the boundary layer winds, see discussion in section 6). In general, air parcels far away from the eyewall would have a longer time interval to gain energy from the ocean as they spiral inward towards the eyewall than those initially close to the eyewall. To quantify this, we performed a number of trajectory calculations and the corresponding Lagrangian θ_e budgets with the results shown in Fig. 11. As is expected, the reduction in $\overline{\theta}_e$ increases with the initial radial distance of the air parcel from the eyewall region. For the case with a cutoff of the surface entropy fluxes outside the radius of 30 km discussed above, the $\overline{\theta}_e$ of an air parcel initially located at a radial distance between 105 km and 130 km is reduced by 2-2.5 K at the time when it enters the eyewall while that of an air parcel initially located between 40 km and 90 km is reduced by less than 1 K (Fig. 11). Further, the reduction in $\overline{\theta}_e$ considerably decreases as the radius outside which the surface entropy fluxes are ignored in the budget increases. Comparing the results for the cutoff of the surface entropy fluxes outside the radii of 40 km, 50 km, and 60 km in the

Lagrangian θ_e budget (Fig. 11), we can see that the surface entropy fluxes between 30-40 km radii would have a considerable effect on the energy budget in the eyewall. This is consistent with the result shown in Fig. 8 and will be discussed further in section 5b. Note that the large reduction in θ_e for the air parcels initially located beyond 105 km from the storm center is mainly due to the long travel time before the parcels reach the eyewall region.

b. A control volume θ_e budget

The Lagrangian θ_e budgets discussed in section 5a only show how the θ_e value for an air parcel could be affected by the surface entropy fluxes outside the eyewall as it travels toward the eyewall following the boundary layer inflow. The results demonstrate qualitatively that the inward energy transport from outside of the eyewall region should contribute to the energy budget in the eyewall. To quantify such a contribution, we conducted a control volume mass-weighted θ_e (namely $\rho\theta_e$) budget, as done by BR09 in their axisymmetric TC model analysis. The volume-integrated form of Eq. (15) for a stationary control volume can be obtained by using the following relationship,

$$\frac{\partial}{\partial t}\left(\int_V \rho A dV\right) = \int_V \rho \frac{dA}{dt} dV - \int_S (\rho A \vec{V}) \bullet \vec{n} dS \,, \qquad (19)$$

where A denotes a physical variable; V represents the control volume; S represents the lateral surfaces of the control volume; $\vec{V}$ are the vector winds in three dimensions; and $\vec{n}$ denotes the unit vector outward normal to the volume surface. Note that the full compressible mass continuity equation is used to derive the second term on the right hand side of (19). Replacing A with θ_e and substituting (15) into (19), we have

$$\frac{\partial}{\partial t}\left(\int_V \rho\theta_e dV\right)=\int_V \rho\left[D_{\theta e}+F_{\theta e}+\frac{1}{C_p\Pi}(D_H+R_H)\right]dV-\int_S(\rho\theta_e\vec{V})\bullet\vec{n}dS\,, \qquad (20)$$

Equation (20) indicates that the change of the volume-integrated, mass-weighted θ_e is determined by the net flux across the lateral and top boundaries of the control volume (the second term on the rhs, including fluxes across the lateral and top boundaries, respectively, FLXL and FLXT) and the various sources (the first term on the rhs) consisting of the horizontal diffusion (HD), vertical mixing (VD, which includes the surface entropy flux), dissipative heating (DH), and radiative cooling (RC).

We conducted a control volume budget analysis to understand the importance of the lateral transport to the mass-weighted θ_e budget in the lower part of the eyewall of the simulated storm. The budget analysis was conducted on the control experiment with the focus on the quasi-steady evolution stage. The control volume θ_e budget was calculated for the period from 144 h to 192 h of simulation, the same period analyzed for the mean Lagrangian θ_e budget analysis discussed in section 5a. The control volume in our budget is defined as a cylinder with its top at 2800 m and its lateral boundary at a radius of 30 km from storm center, corresponding to the location of the eyewall. During this period, the volume-integrated, mass-weighted θ_e in the cylinder showed some small fluctuations around a value of 267.5×10^{13} K kg (266.6×10^{13}–268×10^{13} K kg), consistent with a quasi-steady evolution of the simulated storm. Figure 12 shows the azimuthal mean radial-height distributions of θ_e and radial and vertical flow averaged over the budget period. High θ_e occurs in the eye near the surface. The eyewall ascents appear between 17.5 km and 22.5 km radii in the defined control volume. Strong inflow is limited below

about 1 km in the boundary layer.

Figure 13 shows the results averaged between 144 h to 192 h of simulation based on 3 hourly control volume budgets. The upward θ_e flux at the top of the control cylinder (904.69 K kg s^{-1}) is largely balanced by the lateral inward θ_e flux at the lateral surface of the control cylinder (899.51 K kg s^{-1}). The contribution by the surface entropy flux at the bottom of the control volume (4.51 K kg s^{-1}) is only about 0.5% of the upward θ_e flux at the top and of the inward θ_e flux across the lateral boundary of the control volume. Both horizontal diffusion (HD) and radiative cooling (RC) contribute negatively to the control volume θ_e budget (-0.01 and -0.17 K kg s^{-1}, respectively) with the former negligible. Dissipative heating (DH) contributes positively to the control volume θ_e budget with a contribution (0.94 K kg s^{-1}) about 21% of that due to surface entropy flux. The local processes within the control volume induce a net positive tendency (5.24 K kg s^{-1}) to the volume-integrated, mass-weighted θ_e. This net positive tendency is nearly offset by the negative tendency due to the net θ_e flux through the lateral and top boundaries of the control volume (Fig. 13). This again is consistent with the quasi-steady evolution of the simulated storm during the budget time period. Note that part of the surface entropy flux is transported upward at the top boundary through vertical mixing. That is why vertical mixing (VD) is about 17.2% smaller than the contribution due to surface flux (FLXS) in Fig. 13.

The effect of the boundary layer θ_e change due to the surface entropy fluxes outside the eyewall region discussed in section 5a on the θ_e budget in the eyewall can be quantified by

introducing a small reduction in surface layer θ_e at the lateral boundary in the control volume budget. Some calculations of the lateral θ_e flux with reduced θ_e at the lateral boundary were conducted. For example, a reduction of only 0.5 K in θ_e in the boundary layer below 1100 m reduced the lateral mass-weighted θ_e flux by 1.39×10^9 K kg s^{-1} (898.11×10^9 K kg s^{-1} versus 899.51×10^9 K kg s^{-1}). Although this is small compared with the inward θ_e flux, it is about 31% of that due to the surface entropy flux (4.51×10^9 K kg s^{-1}) or 26.5% of the total contribution by all local processes in the control volume (5.24×10^9 K kg s^{-1}). If we assume that air entering the eyewall from the inflow boundary layer in the control experiment (Fig. 11) is a mixture of air parcels with different radial origins, the surface entropy fluxes outside the eyewall can result in 0.5-1 K increases in θ_e at a radius of 30 km, the radial location of the eyewall. Therefore, a 0.5 K reduction of θ_e in the budget at the lateral boundary, while a conservative estimation, shows a significant effect on the energy balance in the eyewall, indicating that the surface entropy fluxes outside the eyewall do contribute significantly to the energy budget in the eyewall.

c. A sensitivity experiment

The possible effect of the surface entropy fluxes outside the eyewall on the storm intensity cannot be evaluated based on budget analyses discussed in the last two subsections because the change in energy production outside the eyewall may affect the storm intensity and structure and both in turn may affect the energy production in and outside the eyewall. However, the possible effect of surface entropy fluxes outside the eyewall on the storm intensity can be evaluated based on sensitivity experiments in which all possible feedbacks can be included in the

model integration. Therefore, a sensitivity experiment (OE30) was conducted with the model initialized at 48 h of integration from the control experiment, but with the surface exchange coefficient (and thus the surface entropy flux) linearly reduced from 100% at a radius of 30 km corresponding to the eyewall to zero at and outward of radius 45 km. This sensitivity experiment was thus designed to quantify how significant the energy production outside the eyewall contributes to the maximum intensity of the simulated TC.

The storm intensity evolution in the sensitivity experiment (OE30) is compared with that in the control experiment (CTRL) in Fig. 1. Removal of surface entropy fluxes outside the eyewall almost stopped the intensification of the storm after some initial adjustment in the sensitivity experiment. The maximum azimuthal mean wind speed in the sensitivity experiment is about 13.5% lower than that in the control experiment (59.0 m s^{-1} versus 68.2 m s^{-1}) and the minimum central sea level pressure in the sensitivity experiment is about 26 hPa higher than that in the control experiment. This result demonstrates that energy production outside the eyewall contributes significantly to the maximum intensity of the simulated storm and cannot be ignored in estimating the theoretical TC maximum intensity.

The evolution of the RMW in the sensitivity experiment is compared with that in the control experiment in Fig. 3. The RMW in the sensitivity experiment decreased with time in the first 96 h of simulation after the surface fluxes outside the eyewall was excluded (Fig. 3) and remained 7.5 km afterward, which might be the smallest eye and eyewall the model resolution can reasonably resolve since the RMW is only 3 times the model horizontal grid spacing. The

relatively small inner-core size of the storm in the sensitivity experiment (Fig. 14b) shows some similarity to the so-called midget TCs observed over the western North Pacific (Brand 1972; Merrill 1984; Harr et al. 1996). With the small size of the eyewall and the rapid decrease in the low-level wind speed with radius outside the eyewall (not shown), the storm in the sensitivity experiment experienced a steady weakening after about 156 h of simulation (Fig. 1). This is in sharp contrast to the storm intensity and structure in the control experiment, which exhibited only a slight weakening after 192 h of simulation (Fig. 1) and displayed an RMW and an inner core size which increased with time due to the formation of an annual hurricane structure (Figs. 3 and 14a) as pointed out in section 3 and documented in Wang (2008b). The large difference in the inner-core size of the simulated storms in the sensitivity and control experiments suggests that surface entropy fluxes or energy production outside the eyewall contribute not only to the storm intensity but also to the storm inner-core size. The small inner-core size of the simulated storm in the sensitivity experiment can be explained by the lack of active spiral rainbands outside the eyewall as a result of the removal of surface entropy fluxes outside the eyewall (exactly speaking, outside the radius of 30 km) as recently found in Wang (2009).

Figure 15 shows the radial distributions of the azimuthal mean energy production and frictional dissipation rates from the sensitivity experiment at given times. Note that the thermodynamic efficiency for the storm intensity given the choice of initial sounding is about 34.8%, which is used in the calculation of the energy production rate in the sensitivity experiment. The energy production rate was largely reduced immediately outside the eyewall in

the sensitivity experiment (Fig. 15) compared with that in the control experiment (Fig. 5) and became slightly negative outside a radius of about 45 km due to the radiative cooling. Even though the energy production rate was higher than the frictional dissipation rate after about 156 h of simulation (Fig. 15d), the storm still weakened slowly with time in the sensitivity experiment (Fig. 1). Note that both the energy production and frictional dissipation rates decreased at the same time (Fig. 15d), mainly due to the decrease in the inner-core size of the simulated storm (Fig. 14b).

It seems that there exists a positive feedback between the surface fluxes outside the eyewall and the inner-core size of the storm. Specifically, the removal of the surface fluxes outside the eyewall would reduce the storm intensity, suppress convection outside the eyewall and thus reduce the storm size (Wang 2009). This process reduces the low-level winds in the inner core and thus reduces the surface entropy fluxes, resulting in a further decrease in the inner-core size of the storm. Although this explanation for the small inner-core size of the storm simulated in the sensitivity experiment is plausible, a detailed analysis and a complete understanding are an interesting topic currently under investigation and the results will be reported separately. Nevertheless, the results from the sensitivity experiment further demonstrate that energy production outside the eyewall contributes considerably to both the size and maximum intensity of the TC in the simulation.

6. Discussion

Some issues remain and will be discussed in this section. First, we have evaluated the

energy production and frictional dissipation rates in terms of the azimuthal mean. A direct comparison of our results with the axisymmetric model results of Rotunno and Emanuel (1987), Emanuel (1997), PM03, and BR09 is not straightforward. The simulated storm in this study developed asymmetric flow in the boundary layer (Wang 2007, 2008a, b). As pointed out by Emanuel (2000), although the contribution by the asymmetric component to the volume integrated entropy flux tends to be zero if the exchange coefficient and boundary layer entropy are quasi-symmetric about the storm center, the asymmetric component in the ground-relative flow can have a net contribution to the volume integrated surface frictional dissipation rate, which is a cubic power of the total wind speed. As a result, the frictional dissipation rate could be overestimated compared with that from an axisymmetric model since we calculated the frictional dissipation rate before the azimuthal mean was done. To address this possibility, we recalculated the frictional dissipation rate using all the azimuthal mean quantities. The results show only a small difference inside the eyewall and little difference near the RMW (not shown). This indicates that the difference between P_D and D_S under the eyewall in Fig. 5 does not result from the asymmetric flow in the storm boundary layer in our simulation.

Second, when the model results were compared with the theoretical E-MPI in previous studies (Rotunno and Emanuel 1987; PM03, Emanuel 1995, 1997), the effect of radiative cooling used in the models was not considered in their estimation of the E-MPI. This may overestimate the total energy production and thus reduce the difference between the energy production and frictional dissipation rates under the eyewall. As we can see from Fig. 3, the radiative cooling

rate (RAD) is about 180 W m^{-2} in the inner-core region, which offsets about 6-10% of the surface latent heat flux (LH) under the eyewall during the mature stage of the storm in the control experiment (Fig. 7d). This can explain 20%-25% of the 25% difference between the energy production and the frictional dissipation rates near the RMW in the control experiment.

Third, dissipative heating was considered as an energy source to conserve the total energy (Bister and Emanuel 1998) in our simulation. Bister and Emanuel (1998) found that inclusion of dissipative heating may increase the thermodynamic efficiency by 50% theoretically (roughly from 1/3 to 1/2) and thus increased the maximum near-surface wind speed of the TC by about 20% in their axisymmetric model simulations. As we can see from Fig. 4, the dissipative heating rate does contribute to the energy production rate considerably in our simulation. It accounts for about 20% of the total energy production rate under the eyewall during the period when the storm is at its peak intensity. In a simple calculation we dropped both the dissipative heating and the radiative cooling rates in the energy production but increased the thermodynamic efficiency by 50%, specifically changing ε from $(T_s\text{-}T_0)/T_s$ in (2) to $(T_s\text{-}T_0)/T_0$. Surprisingly, the resulting energy production and frictional dissipation rates were closely balanced near the RMW (not shown). This result however should not be considered robust since the energy production immediately outside the eyewall, while contributing to the eyewall energy budget as demonstrated in section 5, could not be balanced by the local frictional dissipation outside the eyewall (Fig. 5).

Fourth, in Emanuel (1997), the outer radius r_0 in (1) was not defined. Based on his Fig. 3,

r_0 should be somewhere outside the eyewall, encompassing the major spiral rainbands. We show in the control experiment that the area-integrated energy production and frictional dissipation rates become equal within a radius of 37.5 km (Fig. 8). Further outward the energy production rate becomes larger than the frictional dissipation rate, indicating that the balance assumption in (1) should not be too far from the RMW, namely r_0 should be in the range of 2-2.5 times the RMW. The storm in the sensitivity experiment is not very energetic because of its small size and both energy production and frictional dissipation rates are much smaller than those in the control experiment (Fig. 15). The area-integrated energy production and frictional dissipation rates in the sensitivity experiment are balanced under the eyewall (near the radius of 7.5 km) with the former larger than the latter for r_0 immediately outside the RMW (Fig. 16) This balance is consistent with the relatively small and narrow eyewall structure in the sensitivity experiment (Figs. 14 and 15), indicating that the outer radius r_0 should be a function of the inner-core size of a TC. Nevertheless, our results from the control experiment and the budget analysis suggest that energy balance within 2-2.5 times the RMW would be a good choice for the maximum intensity in our simulated storm. Therefore, the storm in the sensitivity experiment may not be able to reach its maximum potential intensity because its inner-core size is too small.

In a complementary experiment (not shown) in which the surface fluxes outside a radius of 45 km was excluded, the model storm reached an intensity comparable to that in the control experiment in the first 72 h of simulation. However, the inner-core size decreased with time and eventually reached an RMW similar to that in the sensitivity experiment discussed in section 5.

The storm in the complimentary experiment also weakened at a rate similar to that shown in Fig. 1 for the storm in the sensitivity experiment. This suggests that the excess energy production outside the inner core region (beyond 2-2.5 times the RMW) might not directly contribute to the maximum intensity of the TC but to the growth of the TC size. The energy production outside the inner core would destabilize the local atmospheric column and promote active convection and the development of outer spiral rainbands. Convective heating in these rainbands would increase the inner-core size as recently investigated by Wang (2009). A better understanding of how the surface entropy fluxes outside the inner-core affect the TC size change is a topic currently under investigation and the results will be reported separately.

Finally, Emanuel (1995) and Bryan and Rotunno (2009b) show the dependence of the model TC maximum intensity on the ratio of surface exchange and drag coefficients (C_k/C_D). In our analysis, we have shown the energy production and the frictional dissipation rates directly from the model output. Therefore, the effect of the ratio of surface exchange and drag coefficients did not appear explicitly in our analysis. However, it is unlikely our results will be affected by the wind speed dependent ratio between surface exchange and drag coefficients. As we can see from Fig. 4, the ratio in the sensitivity experiment is larger than that in the control experiment under the respective eyewalls of the simulated storms but the storm in the former experiment is weaker. In a recent study, Bryan and Rotunno (2009b) reported that the effect of the ratio between surface exchange and drag coefficients on the maximum TC intensity is less important than has been believed previously while the maximum intensity of the simulated storm

in their axisymmetric model is most sensitive to the intensity of unresolved turbulence in the radial direction. The results from this study suggest that the storm maximum intensity in a three-dimensional model are more sensitive to the radial distribution of surface entropy fluxes in the inner-core region of the storm than to the ratio between surface exchange and drag coefficients. Since the radial distribution of inner-core surface entropy fluxes is closely related to the boundary layer winds and thus the inner-core structure of a TC, an improved theory for TC maximum potential intensity should include the storm size parameter and the inner-core structure.

7. Summary

The energy production and frictional dissipation rates in a numerically simulated TC were analyzed in this study to evaluate the approximation used in obtaining the theoretical maximum potential intensity (MPI) formulated by Emanuel (1997). The approximation was based on an assumption that the energy production rate and surface frictional dissipation rate are balanced near the radius of maximum wind (RMW) at the time when the storm reaches its MPI (E-MPI). Our results show that the surface frictional dissipation rate in a numerically simulated mature TC is about 25% higher than the energy production rate near the RMW, indicating that the local balance hypothesis used in Emanuel (1997) would underestimate the maximum intensity of a TC. In contrast, the surface frictional dissipation rate is much lower than the energy production rate outside the eyewall. This implies that the excess frictional dissipation under the eyewall should be partially balanced by the energy production outside the eyewall. We show that

the area-integrated energy production and surface frictional dissipation rates are balanced in at a radius of 37.5 km in the mature stage of the simulated storm in the control experiment, suggesting that the energy production within about 2-2.5 times the RMW outside the eyewall is also critical to the maximum intensity of the simulated TC.

To understand how the energy production outside the eyewall contributes to the eyewall energy budget, we calculated both a Lagrangian θ_e budget and a control volume mass-weighted θ_e ($\rho\theta_e$) budget for the quasi-steady stage of the simulated storm in the control experiment. The results show that an air parcel in the surface layer inflow can gain considerable energy from the underlying ocean due to surface entropy flux as it spirals cyclonically inward toward the eyewall. Removal of surface entropy fluxes outside the eyewall result in a reduction of between 0.2-2.5 K in θ_e for an air parcel in the boundary layer inflow entering the eyewall. The actual magnitude depends on the initial radial location of the air parcel and the radius outside which surface entropy fluxes are removed. If the air entering the eyewall in the inflow boundary layer is assumed to be a mixture of air parcels with different radial origins, results from the control experiment showed the surface entropy fluxes outside the eyewall can result in a 0.5-1 K increase in θ_e at a radius of about 30 km from storm center.

The control volume mass-weighted θ_e budget for the lower part of the eyewall volume below 2800 m and within a radius of 30 km from the storm center indicates that the upward flux at the top of the volume is largely balanced by the inward flux across the lateral surface of the eyewall volume. It is found that the contribution by the surface entropy flux to the eyewall θ_e

budget within a radius of 30 km is only about 0.5% of the lateral inward mass-weighted θ_e flux. As a result, a small change in θ_e of the air entering the eyewall in the boundary layer inflow considerably affects the energy budget in the eyewall. Our sensitivity calculation revealed that a 0.5 K reduction in θ_e for air entering the eyewall reduced the inward θ_e flux by as large as 31% of that due to the surface entropy flux under the eyewall or about 26.5% of the total contribution by the local non-conservative processes. This demonstrates that even a small reduction in the θ_e of air entering the eyewall would have a significant effect on the eyewall energy budget because the volume of air outside the eyewall is considerably larger than the volume of the eyewall itself, in sharp contrast to the comparatively small volume of high θ_e air in the eye (BR09).

The budget results are further verified in a sensitivity numerical experiment in which the surface entropy fluxes are eliminated outside a radius of 30-45 km. This leads to a 13.5% reduction of the maximum intensity of the model TC, further demonstrating that energy production outside the eyewall contributes considerably to the maximum intensity of a TC. Therefore, the underestimation of the model TC maximum intensity by the E-MPI is partly due to the approximation of a local balance between the energy production rate and frictional dissipation rate near the RMW. In agreement with BR09, this underestimation by E-MPI is not due to ignoring the effect of the near-surface high entropy air in the eye, which otherwise could provide surplus energy to the eyewall as suggested by Persing and Montgomery (2003). Results from this study demonstrate that the underestimation by E-MPI of the maximum intensity of the simulated TC is primarily due to ignoring energy production outside the eyewall as energy

production within about 2-2.5 times the RMW is required to balance the surface frictional dissipation under the eyewall. Results from our sensitivity experiments also show that energy production outside the eyewall is critical not only to the maximum intensity but also to the inner-core size of the simulated storm.

Since the distribution of energy production rate is largely determined by the distribution of the boundary layer winds of the storm itself, the maximum intensity of a TC could be modified by the storm structure and inner-core size as implied in our sensitivity experiments. In the E-MPI, the TC maximum intensity does not depend on the inner-core size or structure of the storm itself. This observation needs to be examined in a future study. We found a strong dependence of the simulated storm size on surface entropy fluxes outside the eyewall. A detailed study to understand how the simulated TC size and intensity depend on the radial distribution of surface entropy fluxes is a topic currently under investigation and the results will be reported in a future publication.

Acknowledgments: The authors are grateful to three anonymous reviewers and Tom Dunn whose comments and suggestions helped improve the manuscript. This study has been supported by NSF grant ATM-0427128 and ATM-0754039 and ONR grant 00014-06-10303. Additional support has been provided by the JAMSTEC, NASA, and NOAA through their sponsorships of the International Pacific Research Center (IPRC) in the School of Ocean and Earth Science and Technology (SOEST) at the University of Hawaii.

References

Bell, M. M., and M. T. Montgomery, 2008: Observed structure, evolution, and potential intensity of category 5 Hurricane Isabel from 12 to 14 September. *Mon. Wea. Rev*., **136**, 2023-2046.

Bister, M., and K. A. Emanuel, 1998: Dissipative heating and hurricane intensity. *Meteor. Atmos. Phys*., **65**, 233-240.

Brand, S., 1972: Very large and very small typhoons of the western North Pacific Ocean. *J. Meteor. Soc. Japan*, **50**, 332-341.

Bryan, G. H., and R. Rotunno, 2009a: The influence of near-surface, high-entropy air in hurricane eyes on maximum hurricane intensity. *J. Atmos. Sci*., **66**, 148-158.

Bryan, G. H., and R. Rotunno, 2009b: The maximum intensity of tropical cyclones in axisymmetric numerical model simulations. *Mon. Wea. Rev*., in press.

Bryan, G. H., and R. Rotunno, 2009c: Evaluation of an analytical model for the maximum intensity of tropical cyclones. *J. Atmos. Sci*., in press.

Cram, T. A., J. Persing, M.T. Montgomery, and S.A. Braun, 2007: A Lagrangian trajectory view on transport and mixing processes between the eye, eyewall, and environment using a high-resolution simulation of Hurricane Bonnie (1998). *J. Atmos. Sci*., **64**, 1835-1856.

Emanuel, K. A., 1986: An air-sea interaction theory of tropical cyclones. Part I: Steady-state maintenance. *J. Atmos. Sci*., **43**, 585-604.

Emanuel, K. A., 1988: The maximum intensity of hurricanes. *J. Atmos. Sci*., **45**, 1143-1155.

Emanuel, K. A., 1991: The theory of hurricanes. *Annu. Rev. Fluid Mech*., **23**, 179-196.

Emanuel, K. A., 1995: Sensitivity of tropical cyclones to surface exchange coefficients and a revised steady-state model incorporating eye dynamics. *J, Atmos. Sci*., **52**, 3969-3676.

Emanuel, K. A., 1997: Some aspects of hurricane inner-core dynamics and energetic. *J. Atmos. Sci*., **54**, 1014-1026.

Emanuel, K. A., 2000: A statistical analysis of hurricane intensity. *Mon. Wea. Rev*., **128**, 1139-1152.

Fairall, C. W., E. F. Bradley, J. E. Hare, A. A. Grachev, and J. B. Edson, 2003: Bulk parameterization of air–sea fluxes: Updates and verification for the COARE algorithm. *J. Climate, 16*, 571–591.

Gray, W. M., E. Ruprecht, and R. Phelps, 1975: Relative humidity in tropical weather systems. *Mon. Wea. Rev.*, **103**, 685-690.

Harr, P. A., M. R. Kalafsky, and R. Elsberry, 1996: Environmental conditions prior to formation of a midget tropical cyclone during TCM-93. *Mon. Wea. Rev*., **124**, 1693-1710.

Knaff, J.A., J.P. Kossin, and M. DeMaria, 2003: Annular hurricanes, *Wea. Forecasting*, **18**, 204-223.

Langland, R. H., and C.-S. Liou, 1996: Implementation of an E-ε parameterization of vertical subgrid-scale mixing in a regional model. *Mon. Wea. Rev.*, **124**, 905-918.

Malkus, J. S., and H. Riehl, 1960: On the dynamics and energy transformations in steady-state hurricane. *Tellus,* **12**, 1-20.

Merrill, R. T., 1984: A comparison of large and small tropical cyclones. *Mon. Wea. Rev*., **112**,

1408-1418.

Montgomery, M. T., M. M. Bell, S. D. Aberson, and M. L. Black, 2006: Hurricane Isabel (2003): New insights into the physics of intense storm. Part I: Mean vortex structure and maximum intensity estimates. *Bull. Amer. Meteor. Soc*., **87**, 1335-1347.

Persing, J., and M. T. Montgomery, 2003: Hurricane superintensity. *J. Atmos. Sci.*, **60**, 2349-2371.

Persing, J., and M. T. Montgomery, 2005: In environmental CAPE important in the determination of maximum possible hurricane intensity? *J. Atmos. Sci*., **62**, 542-550.

Rotunno, R., and K. A. Emanuel, 1987: An air-sea interaction theory for tropical cyclones. Part II: Evolutionary study using a non-hydrostatic axisymmetric model. *J. Atmos. Sci*, **44,** 542-561.

Smith, R. K., M. T. Montgomery, and S. Vogl, 2008: A critique of Emanuel's hurricane model and potential intensity theory. *Q. J. R. Meteorol. Soc*., **134**, 551-561.

Wang, Y., 2001: An explicit simulation of tropical cyclones with a triply nested movable mesh primitive equation model: TCM3. Part I: Model description and control experiment. *Mon. Wea. Rev*., **129,** 1370-1394.

Wang, Y., 2002a: Vortex Rossby waves in a numerically simulated tropical cyclone. Part I: Overall structure, potential vorticity and kinetic energy budgets. *J. Atmos. Sci.,* **59**, 1213-1238.

Wang, Y., 2002b: Vortex Rossby waves in a numerically simulated tropical cyclone. Part II: The

role in tropical cyclone structure and intensity changes. *J. Atmos. Sci.,* **59**, 1239-1262.

Wang, Y., 2002c: An explicit simulation of tropical cyclones with a triply nested movable mesh primitive equation model-TCM3 Part II: Model refinements and sensitivity to cloud microphysics parameterization. *Mon. Wea. Rev.*, **130**, 3022-3036.

Wang, Y., 2007: A multiply nested, movable mesh, fully compressible, nonhydrostatic tropical cyclone model - TCM4: Model description and development of asymmetries without explicit asymmetric forcing. *Meteor. Atmos. Phys*., 97, 93-116.

Wang, Y., 2008a: Rapid filamentation zone in a numerically simulated tropical cyclone. *J. Atmos. Sci.*, **65**, 1158-1181.

Wang, Y., 2008b, Structure and formation of an annular hurricane simulated in a fully compressible, nonhydrostatic model–TCM4. *J. Atmos. Sci.*, 65, 1505-1527.

Wang, Y., 2009: How do outer spiral rainbands affect tropical cyclone structure and intensity? *J. Atmos. Sci.*, **66**, 1250–1273.

Yang, B., Y. Wang, and B. Wang, 2007: The effect of internally generated inner-core asymmetries on tropical cyclone potential intensity. *J. Atmos. Sci*., **64**, 1165-1188.

Figure captions

Figure 1. Time evolution of (a) the maximum azimuthal mean wind speed (m s^{-1}) at the lowest model level (35.6 m above the sea surface) and (b) the minimum central surface pressure (hPa) in the control experiment (CTRL, solid) and the sensitivity experiment (OE30, dashed, see section 5).

Figure 2. Axisymmetric structure of the simulated tropical cyclone after 168 h of integration in the control experiment. (a) Tangential wind speed (m s^{-1}); (b) radial wind speed (m s^{-1}); (c) vertical wind speed (m s^{-1}); (d) perturbation temperature (K); (e) potential vorticity (PVU); and (e) equivalent potential temperature (K).

Figure 3. Time evolution of the radius of maximum wind (RMW in km) in the control experiment (CTRL, solid) and in the sensitivity experiment with surface fluxes outside the eyewall eliminated (OE30, dashed).

Figure 4. Radial distributions of the ratio of exchange and drag coefficients (C_k/C_D) averaged between 144 and 192 h of simulation in the control experiment and between 72 and 96 h of simulation in the sensitivity experiment in which the exchange coefficient is reset to decrease linearly from 30 km radius to 0 at and outward of radius 45 km

Figure 5. Radial distributions of the azimuthal mean mechanical dissipation rate (W m^{-2}, solid) and the azimuthal mean total energy production rate (W m^{-2}, dashed) in the control experiment at given times and time mean.

Figure 6. Radial distribution of the difference (W m^{-2}) between the energy production rate (P_D) and the frictional dissipation rate (D_S) at 24h, 60h, 72h, and 144-192h average of simulation.

Figure 7. Radial distribution of the azimuthal mean sensible heat flux (SH), latent heat flux (LH),

dissipative heating (DHT), and radiative cooling (RAD) at given times and time mean. All are in unit W m^{-2}.

Figure 8. Area-integrated energy production rate (10^{12} W, dashed) and surface frictional dissipation rate (10^{12} W, solid) within a given radius of r_0 in the control experiments averaged between 144-192 h of simulation.

Figure 9. Equivalent potential temperature (shaded) and horizontal winds (vectors) averaged in the lowest 1000 m model layer between 144 h and 192 h of model simulation. The white curve shows the trajectory originally located 100 km to the east of the storm center calculated based on the mean winds.

Figure 10. Time series of equivalent potential temperatures (K, left legend) following the parcel along the trajectory as shown in Fig. 9 with the parameterized vertical mixing including surface entropy flux (EPT_SFLX) and without both the parameterized vertical mixing and surface entropy flux outside the radius of 30 km (EPT_NoSFLX). Shown are also the corresponding radial distance (km, right legend) of the air parcel and the local equivalent potential temperature (EPT_Model) at the given time on the trajectory. The thick vertical line slightly after 1.5 hr shows the time when the air parcel enters the eyewall, which is roughly within a radius of 30 km.

Figure 11. Reduction of θ_e (K) for an air parcel which spirals cyclonically inward starting from the given distance (horizontal axis) east of the storm center and following the boundary layer inflow. Surface fluxes and vertical mixing of θ_e are ignored outside the given radius, RE. Four examples are shown for RE = 30, 40, 50, and 60 km.

Figure 12. Radial-height cross-section of the azimuthal mean equivalent potential temperature

averaged between 144 h and 192 h of integration in the control experiment. Arrows (in m s^{-1}) show radial and vertical flow with vertical wind multiplied by a factor of 2. The dashed box indicates the area included in the control-volume θ_e budget.

Figure 13. Results for the control volume entropy budget averaged between 144 h and 192 h of simulation. Shown are lateral inward entropy flux across the cylinder surface at the radius of 30 km (FLXL), upward entropy flux at the top (2.8 km above the sea surface) of the cylinder (FLXT), and surface entropy flux at the base of the cylinder (FLXS). Given are also the entropy changes due to horizontal diffusion (HD), vertical mixing (VD), radiative cooling (RC), and dissipative heating (DH). Note that the vertical mixing (VD) includes the surface entropy flux (FLXS) already. The units are 10^9 K kg s^{-1}. The total volume-integrated entropy in the cylinder experienced some small fluctuations around a value of 267.5×10^{13} K kg, between 266.6×10^{13} and 268×10^{13} K kg during this time period.

Figure 14. Distribution of the surface rain rates (mm h^{-1}) after 24, 72, and 168 h of simulation in the control experiment (a) and the sensitivity experiment (b). Isobars of 980 hPa and 995 hPa of surface pressure are plotted in contours.

Figure 15. Same as in Fig. 5 but for the sensitivity experiment with the surface entropy fluxes eliminated outside the eyewall. Times shown are after 48 h spin-up in the control experiment.

Figure 16. Area-integrated energy production rate (10^{12} W, dashed) and surface frictional dissipation rate (10^{12} W, solid) within a given radius of r_0 after 72 h of simulation in the sensitivity experiment (OE30) with surface entropy fluxes outside the eyewall eliminated.

Table 1. The theoretical E-MPI in terms of near surface maximum wind speed ($\mathbf{V_m}$ and the minimum central sea level pressure P_{min}) calculated with different ratios of exchange coefficient to drag coefficient (C_k/C_D) under assumptions of both reversal (σ=0) and pseudo-adiabatic eyewall ascent (σ=1) for the given SST of 29^{o}C and the mean atmospheric sounding of the clear-sky conditions over tropical western Pacific of Gray et al. (1975), which is used as the unperturbed environmental conditions in the model simulation. Note that the outflow layer temperature (T_0) and the corresponding thermodynamic efficiency (ε) defined by (2) are obtained directly from the output for each E-MPI calculation.

C_k/C_D	Reversal eyewall ascent (σ=0)				Pseudo-adiabatic eyewall ascent (σ=1)			
	V_m (m s^{-1})	P_{min} (hPa)	T_0 (K)	ε (%)	V_m (m s^{-1})	P_{min} (hPa)	T_0 (K)	ε (%)
0.80	67.3	922.5	196.3	35.03	73.2	899.5	195.0	35.46
0.40	46.7	970.0	197.9	34.5	51.1	957.9	195.7	35.23
0.32	41.5	979.6	199.0	34.14	45.5	969.8	196.1	35.10

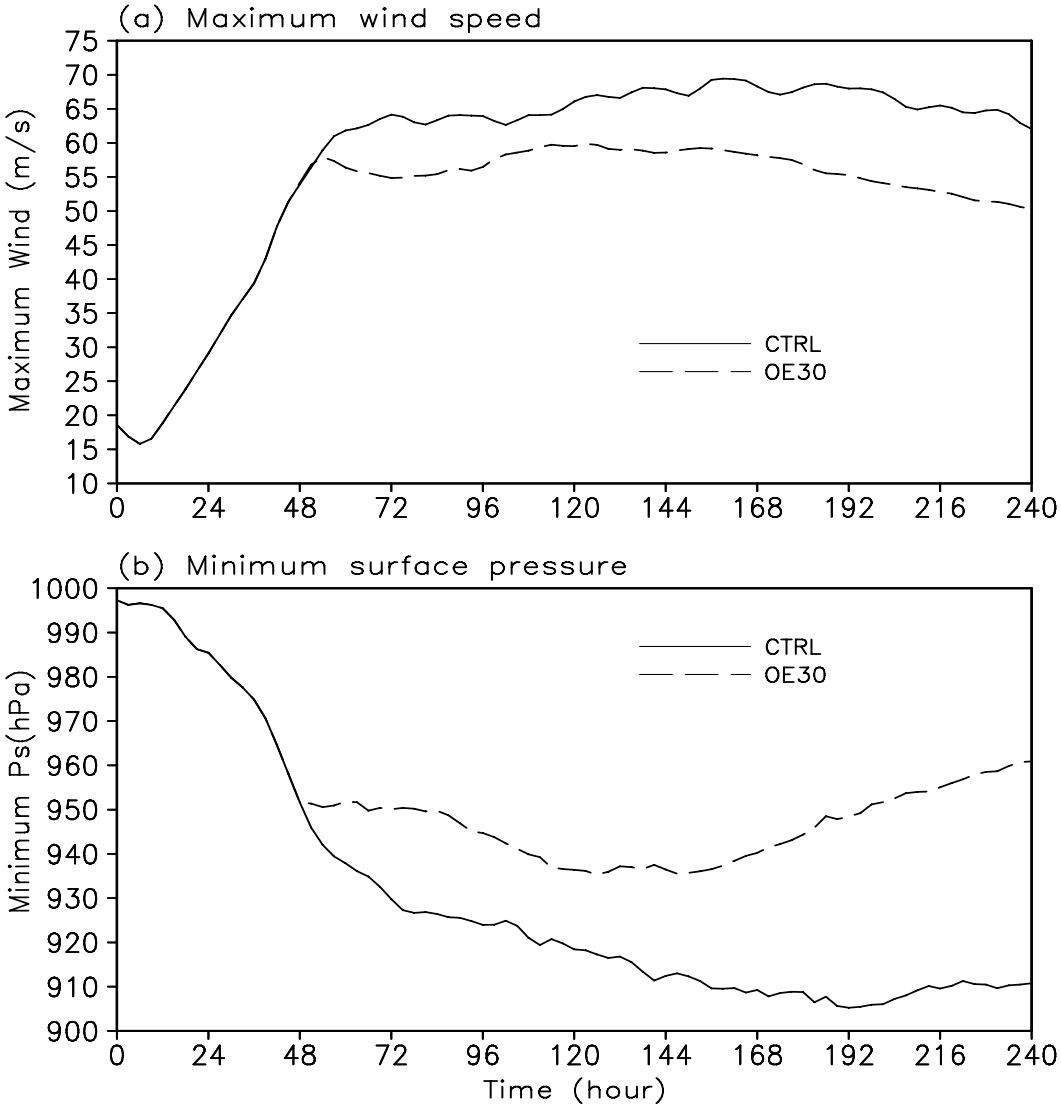

Figure 1. Time evolution of (a) the maximum azimuthal mean wind speed (m s^{-1}) at the lowest model level (35.6 m above the sea surface) and (b) the minimum central surface pressure (hPa) in the control experiment (CTRL, solid) and the sensitivity experiment (OE30, dashed, see section 5).

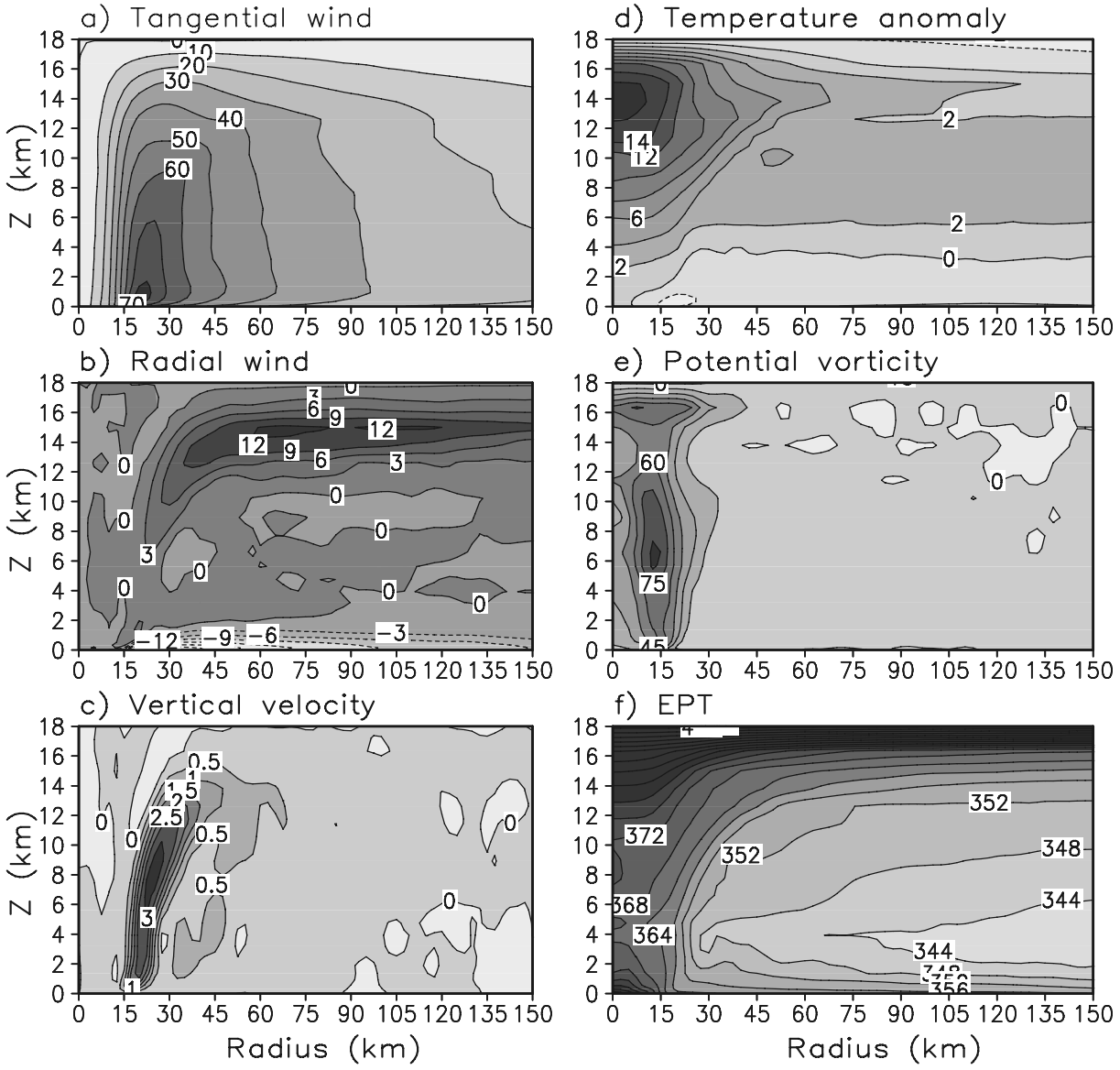

Figure 2. Axisymmetric structure of the simulated tropical cyclone after 168 h of integration in the control experiment. (a) Tangential wind speed (m s^{-1}); (b) radial wind speed (m s^{-1}); (c) vertical wind speed (m s^{-1}); (d) perturbation temperature (K); (e) potential vorticity (PVU); and (e) equivalent potential temperature (K).

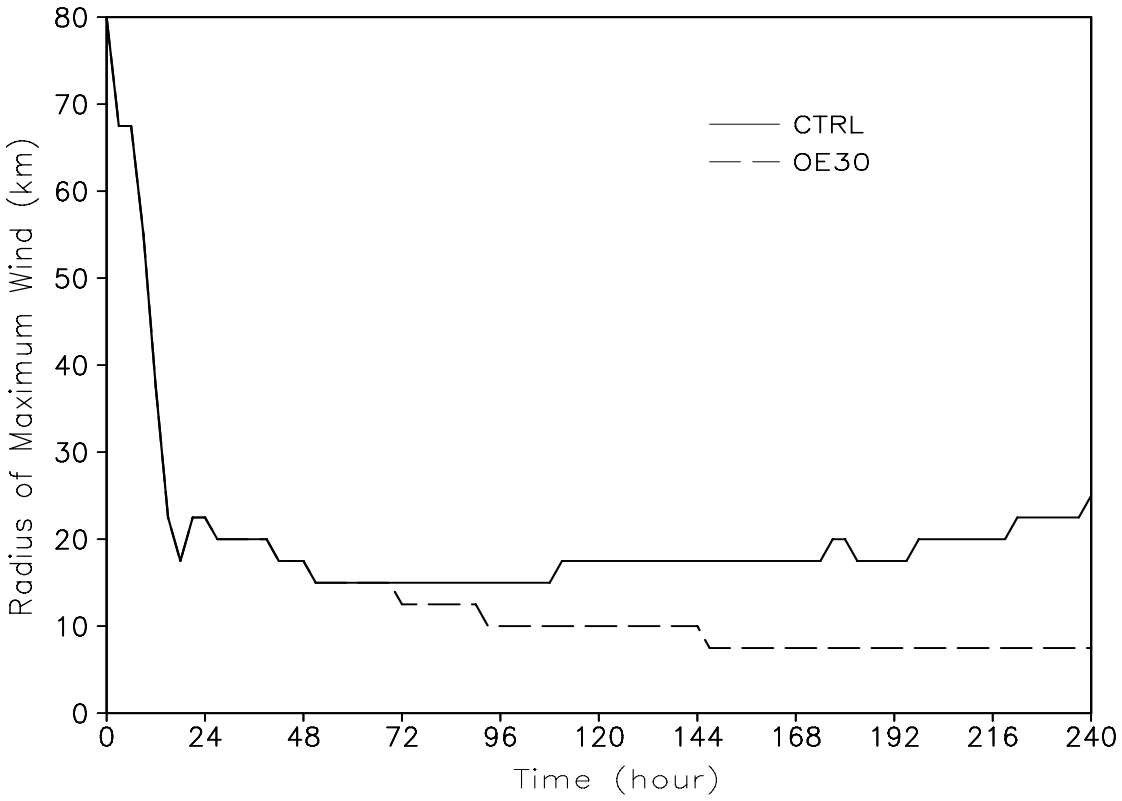

Figure 3. Time evolution of the radius of maximum wind (RMW in km) in the control experiment (CTRL, solid) and in the sensitivity experiment with surface fluxes outside the eyewall eliminated (OE30, dashed).

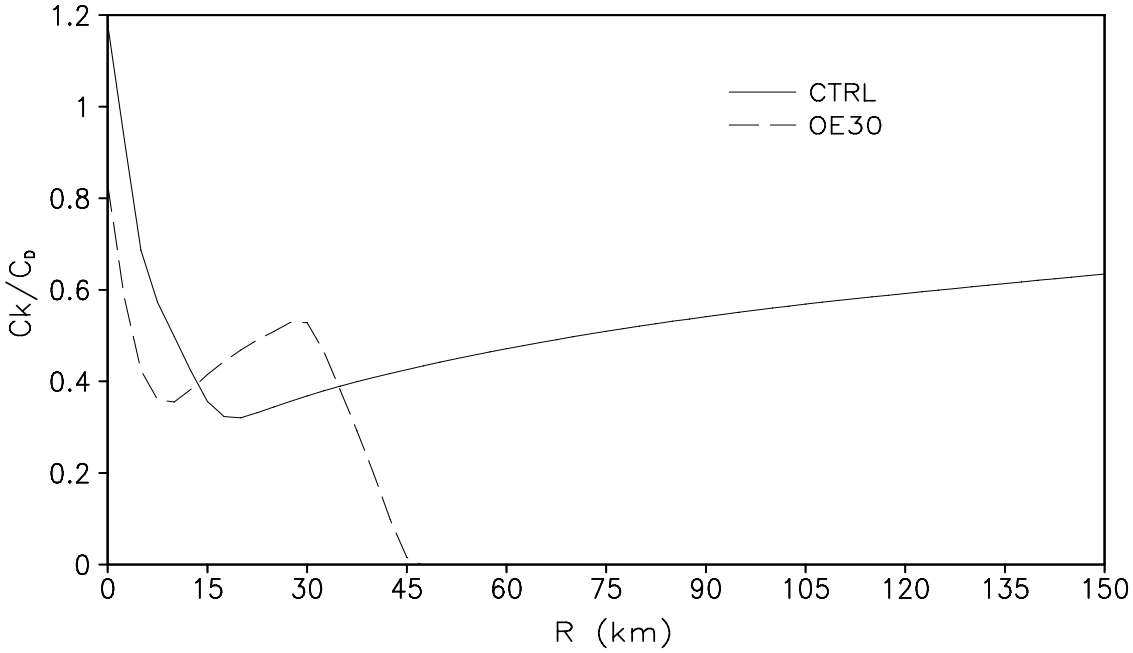

Figure 4. Radial distributions of the ratio of exchange and drag coefficients (C_k/C_D) averaged between 144 and 192 h of simulation in the control experiment and between 72 and 96 h of simulation in the sensitivity experiment in which the exchange coefficient is reset to decrease linearly from 30 km radius to 0 at and outward of radius 45 km.

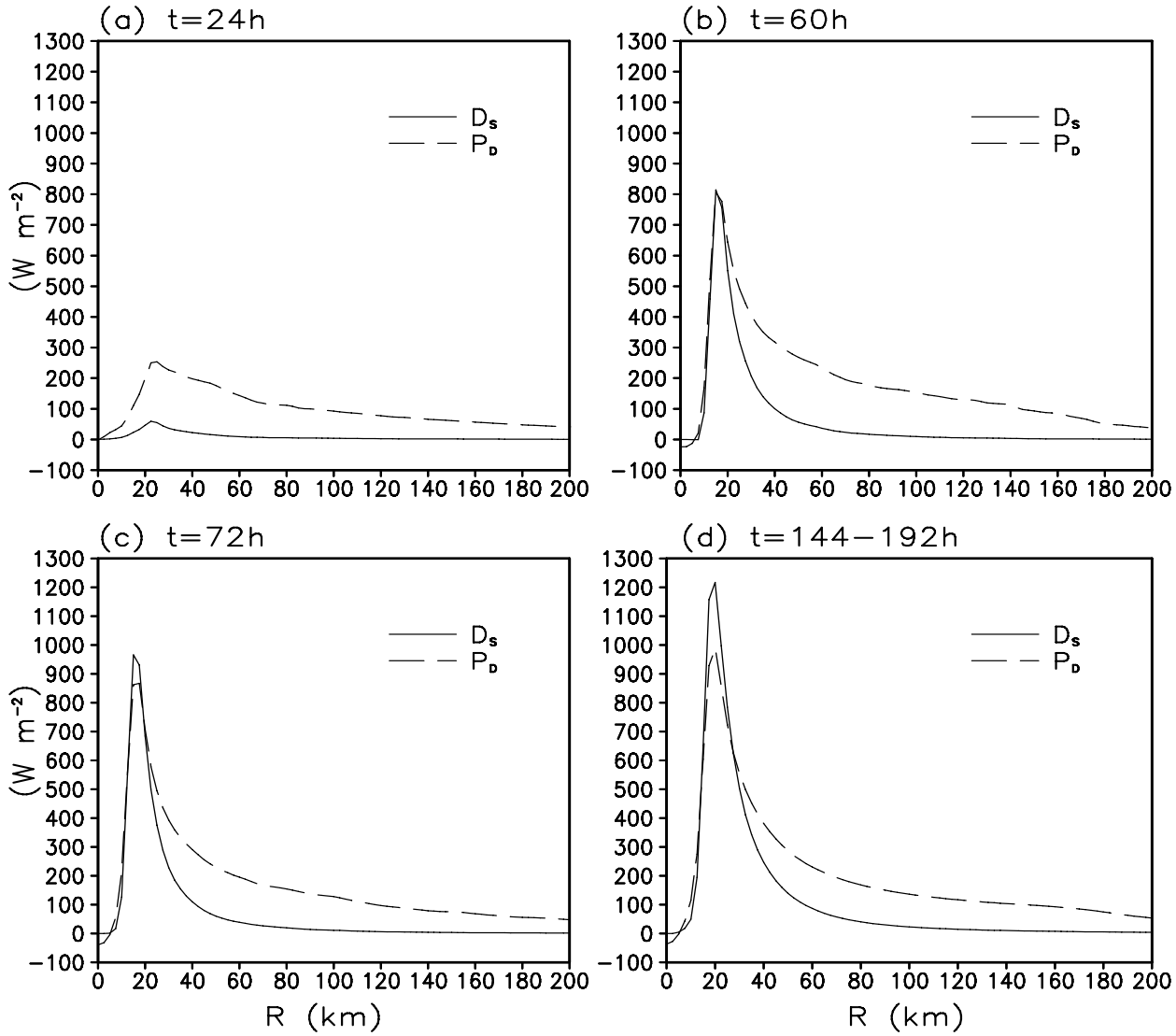

Figure 5. Radial distributions of the azimuthal mean mechanical dissipation rate (D_S, W m^{-2}, solid) and the azimuthal mean total energy production rate (P_D, W m^{-2}, dashed) in the control experiment at given times and time mean.

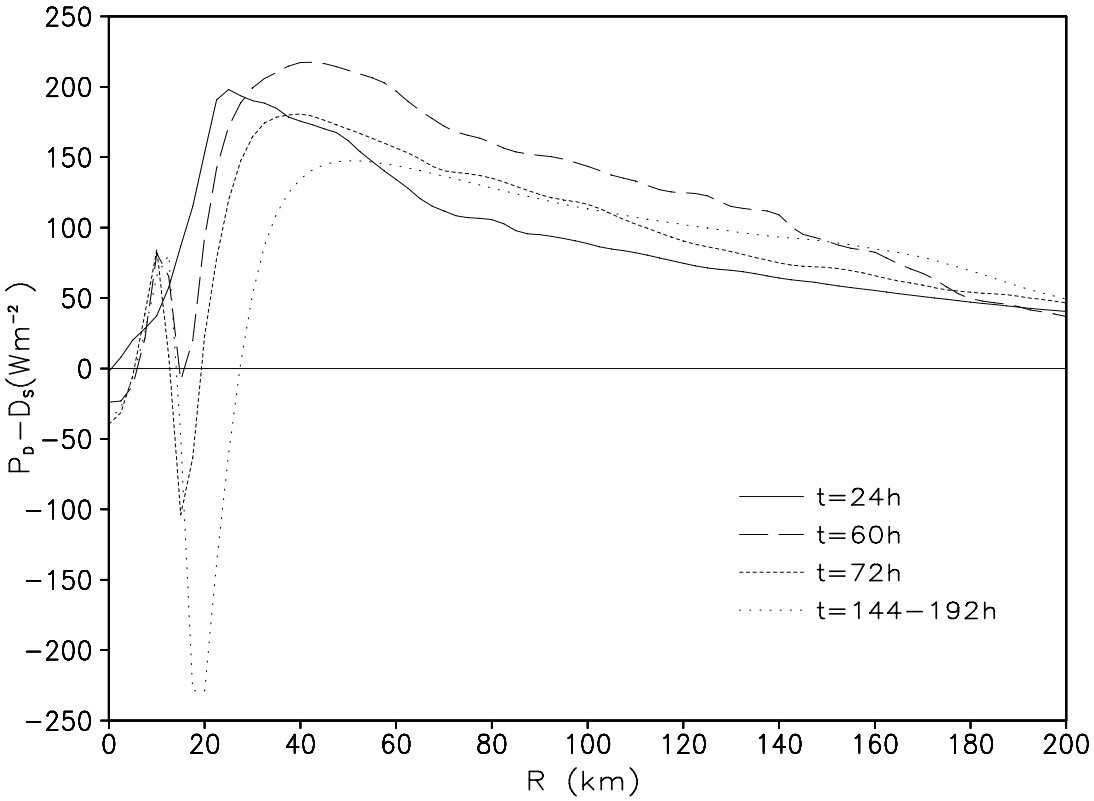

Figure 6. Radial distribution of the difference (W m^{-2}) between the energy production rate (P_D) and the frictional dissipation rate (D_S) at 24h, 60h, 72h, and 144-192h average of simulation.

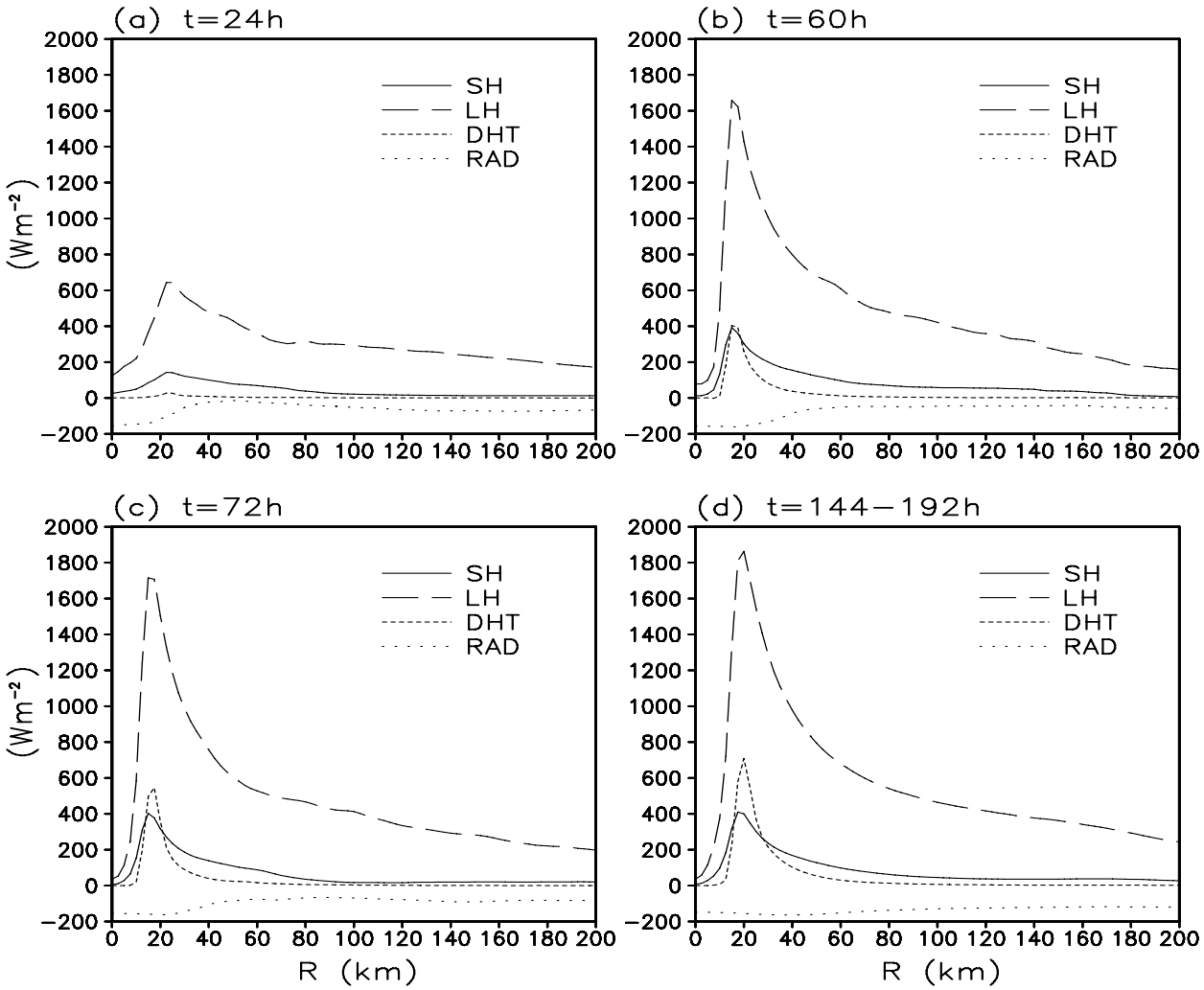

Figure 7. Radial distribution of the azimuthal mean sensible heat flux (SH), latent heat flux (LH), dissipative heating (DHT), and radiative cooling (RAD) at given times and time mean. All are in unit W m^{-2}.

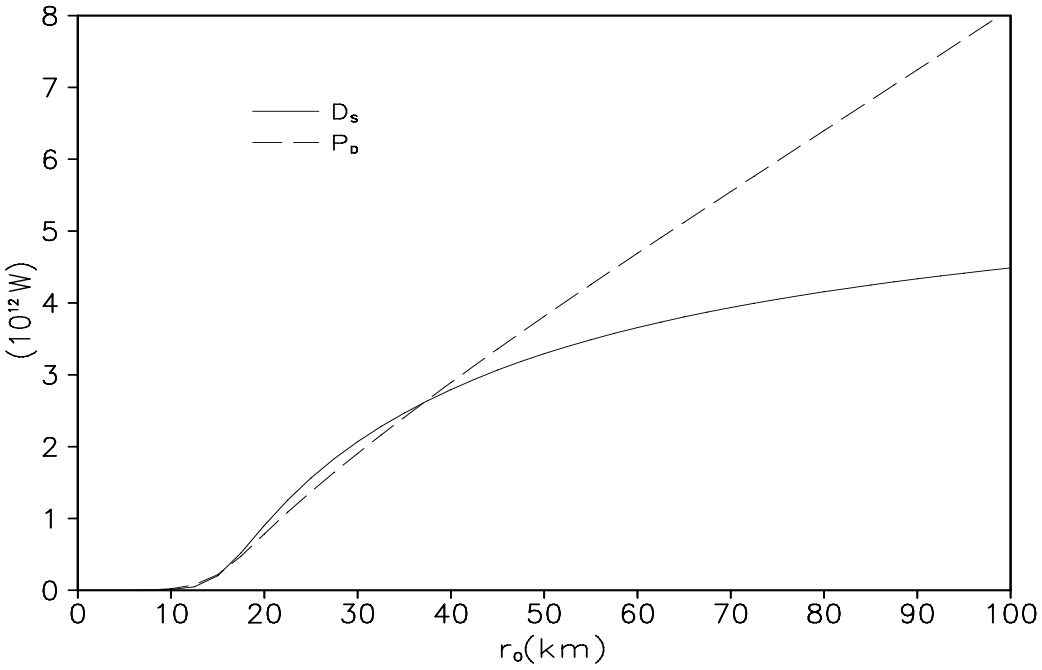

Figure 8. Area-integrated energy production rate (10^{12} W, dashed) and surface frictional dissipation rate (10^{12} W, solid) within a given radius of r_0 in the control experiments averaged between 144-192 h of simulation.

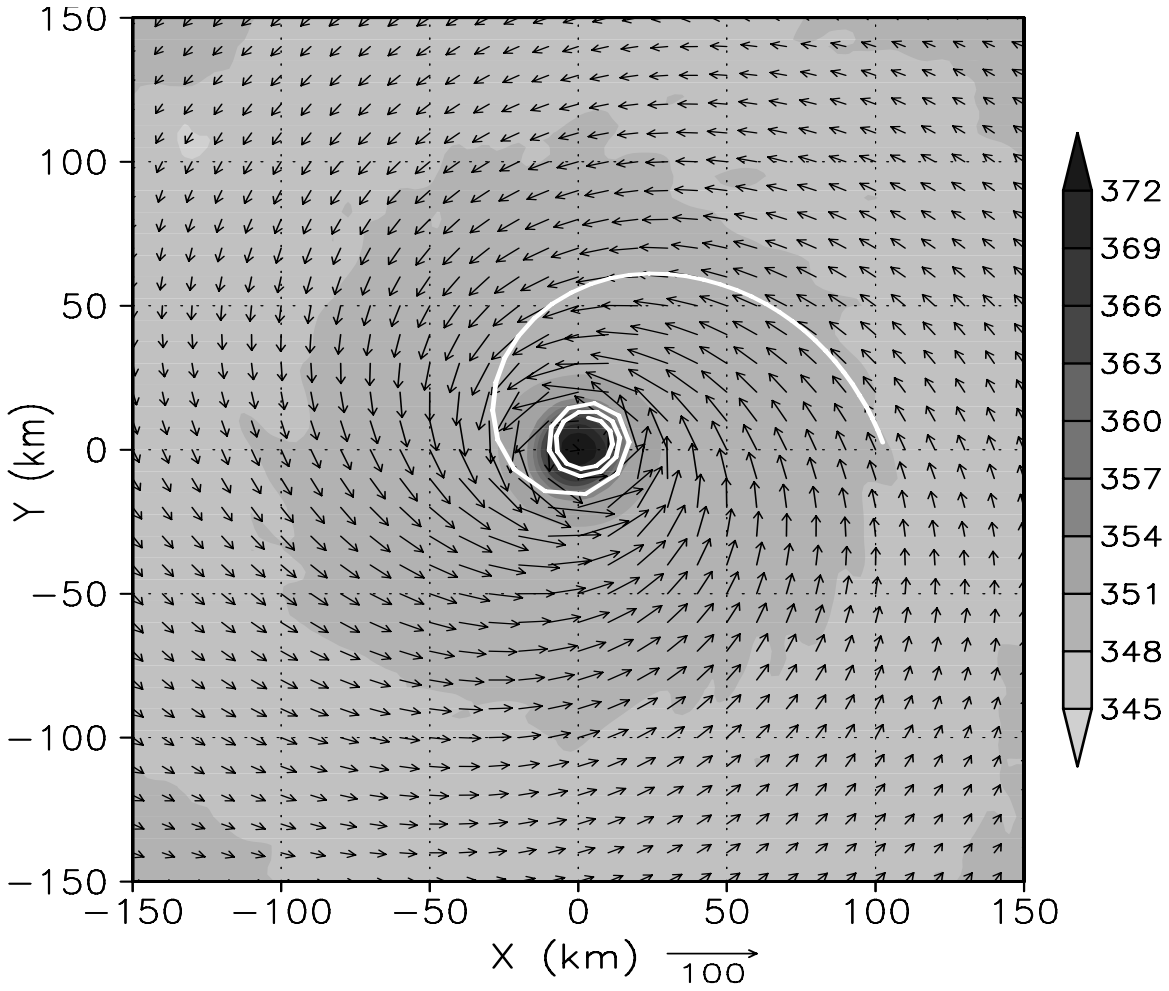

Figure 9. Equivalent potential temperature (shaded) and horizontal winds (vectors) averaged in the lowest 1000 m model layer between 144 h and 192 h of model simulation. The white curve shows the trajectory originally located 100 km to the east of the storm center calculated based on the mean winds.

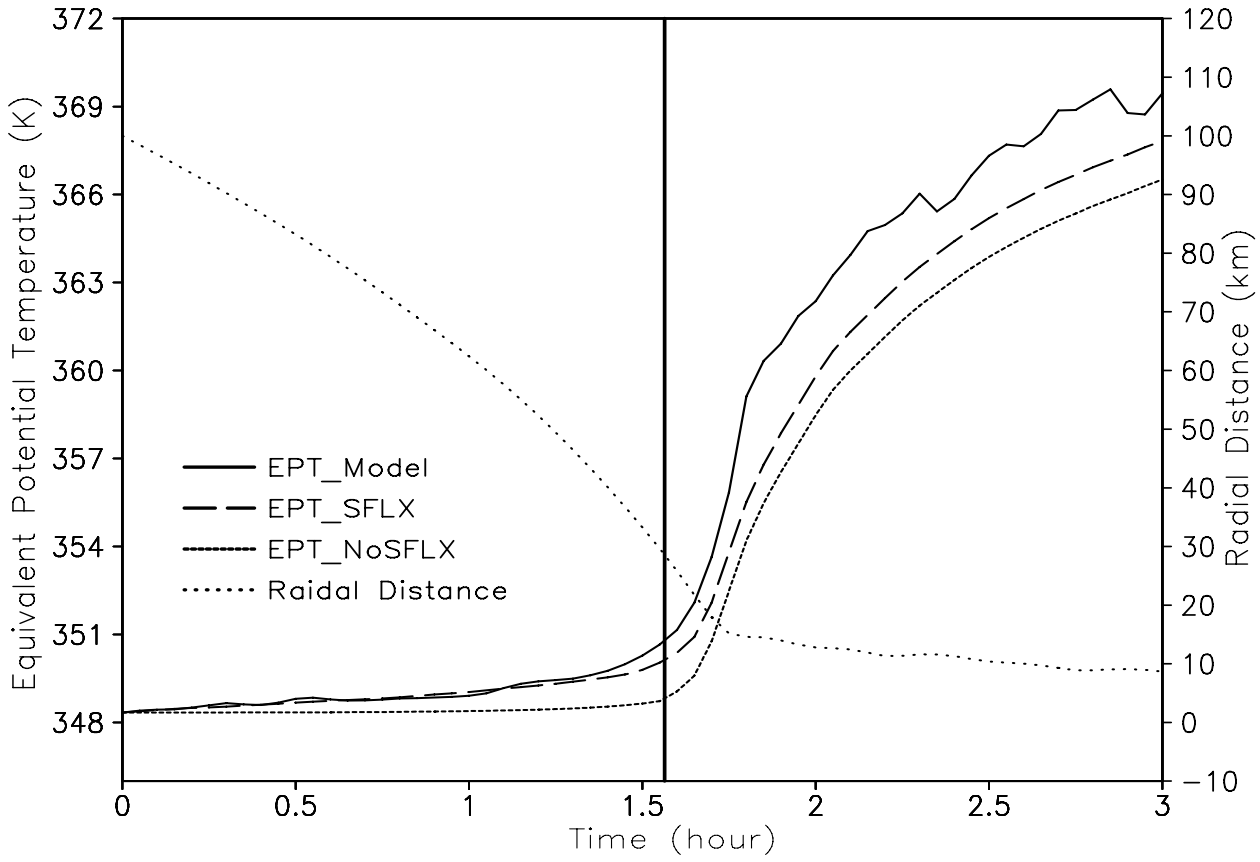

Figure 10. Time series of equivalent potential temperatures (K, left legend) following the parcel along the trajectory as shown in Fig. 9 with the parameterized vertical mixing including surface entropy flux (EPT_SFLX) and without both the parameterized vertical mixing and surface entropy flux outside the radius of 30 km (EPT_NoSFLX). Also shown are the corresponding radial distance (km, right legend) of the air parcel from its starting location and the local equivalent potential temperature (EPT_Model) at the given time on the trajectory. The thick vertical line slightly after 1.5 hr shows the time when the air parcel enters the eyewall, which is roughly within a radius of 30 km.

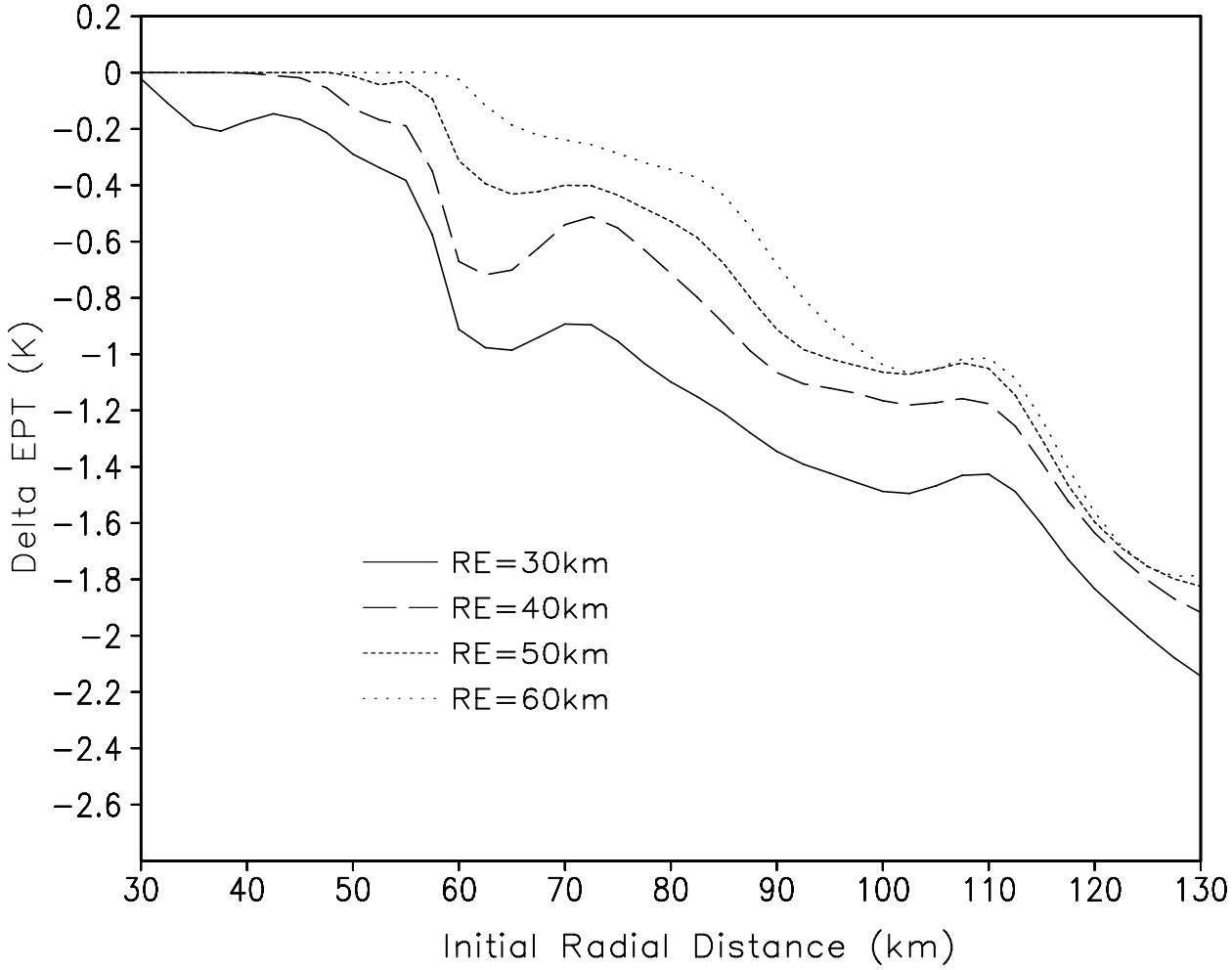

Figure 11. Reduction of θ_e (K) for an air parcel which spirals cyclonically inward starting from the given distance (horizontal axis) east of the storm center and following the boundary layer inflow. Surface fluxes and vertical mixing of θ_e are ignored outside the given radius, RE. Four examples are shown for RE = 30, 40, 50, and 60 km.

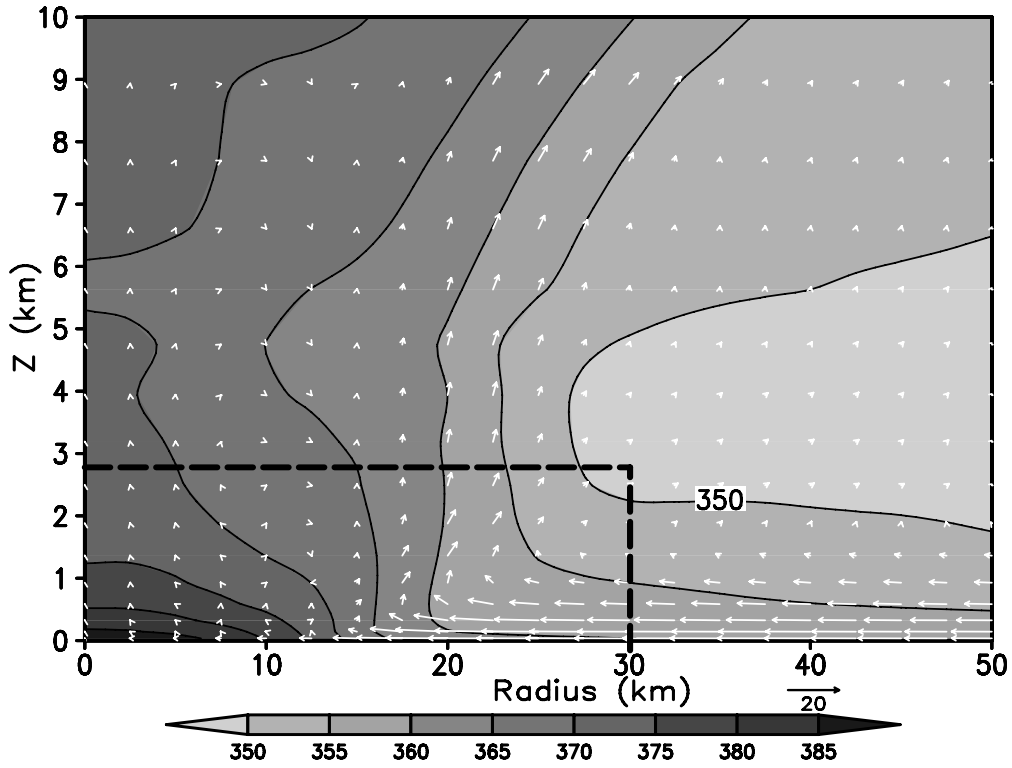

Figure 12. Radial-height cross-section of the azimuthal mean equivalent potential temperature averaged between 144 h and 192 h of integration in the control experiment. Arrows (in m s^{-1}) show radial and vertical flow with vertical wind multiplied by a factor of 2. The dashed box indicates the area included in the control-volume θ_e budget.

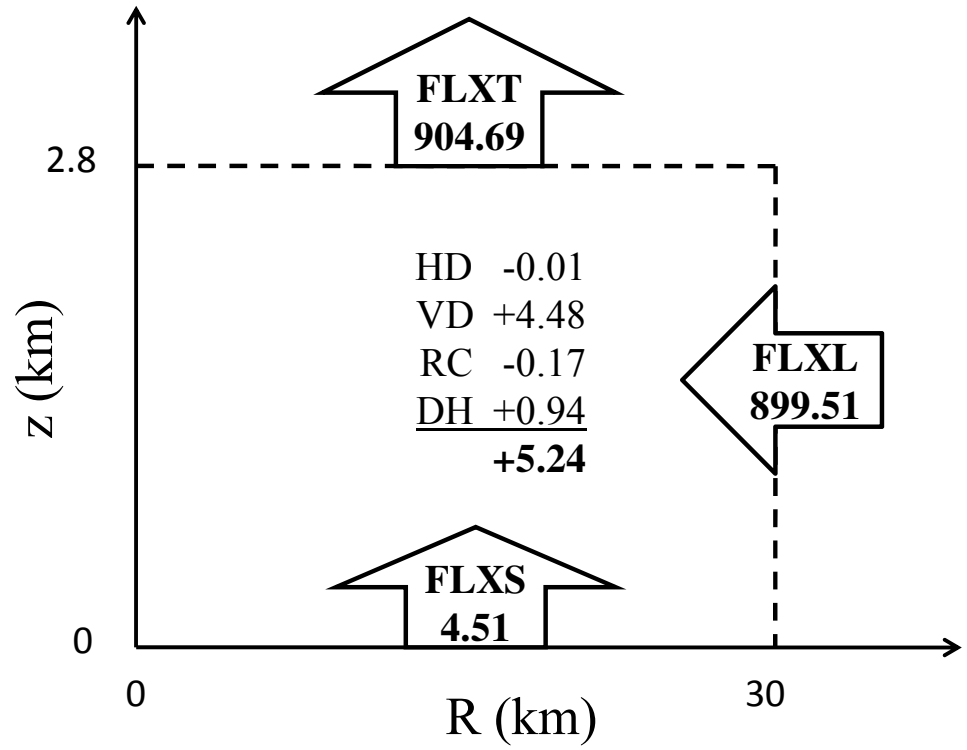

Figure 13. Results for the control volume entropy budget averaged between 144 h and 192 h of simulation. Shown are lateral inward entropy flux across the cylinder surface at the radius of 30 km (FLXL), upward entropy flux at the top (2.8 km above the sea surface) of the cylinder (FLXT), and surface entropy flux at the base of the cylinder (FLXS). Given are also the entropy changes due to horizontal diffusion (HD), vertical mixing (VD), radiative cooling (RC), and dissipative heating (DH). Note that the vertical mixing (VD) includes the surface entropy flux (FLXS) already. The units are 10^9 K kg s^{-1}. The total volume-integrated entropy in the cylinder experienced some small fluctuations around a value of 267.5×10^{13} K kg, between 266.6×10^{13} and 268×10^{13} K kg during this time period.

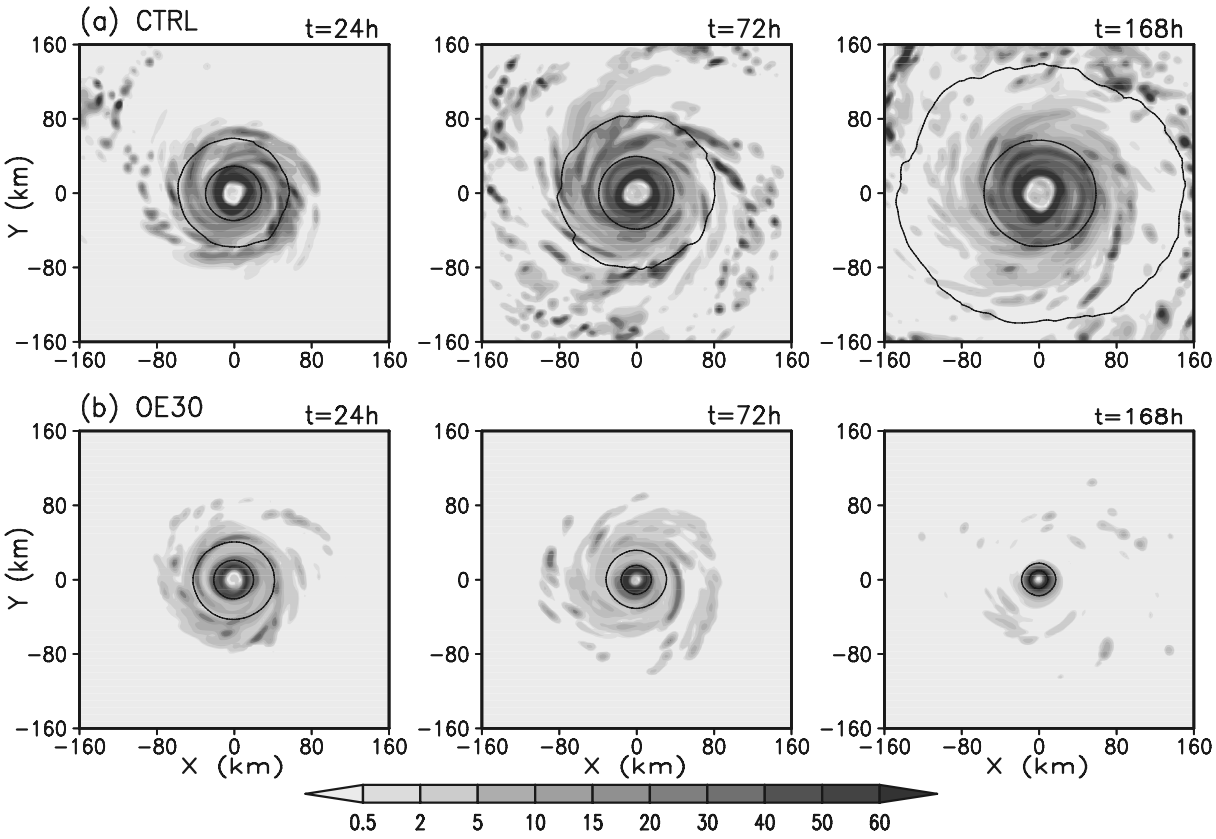

Figure 14. Distribution of the surface rain rates (mm h^{-1}) after 24, 72, and 168 h of simulation in the control experiment (a) and the sensitivity experiment (b). Isobars of 980 hPa and 995 hPa of surface pressure are plotted in contours.

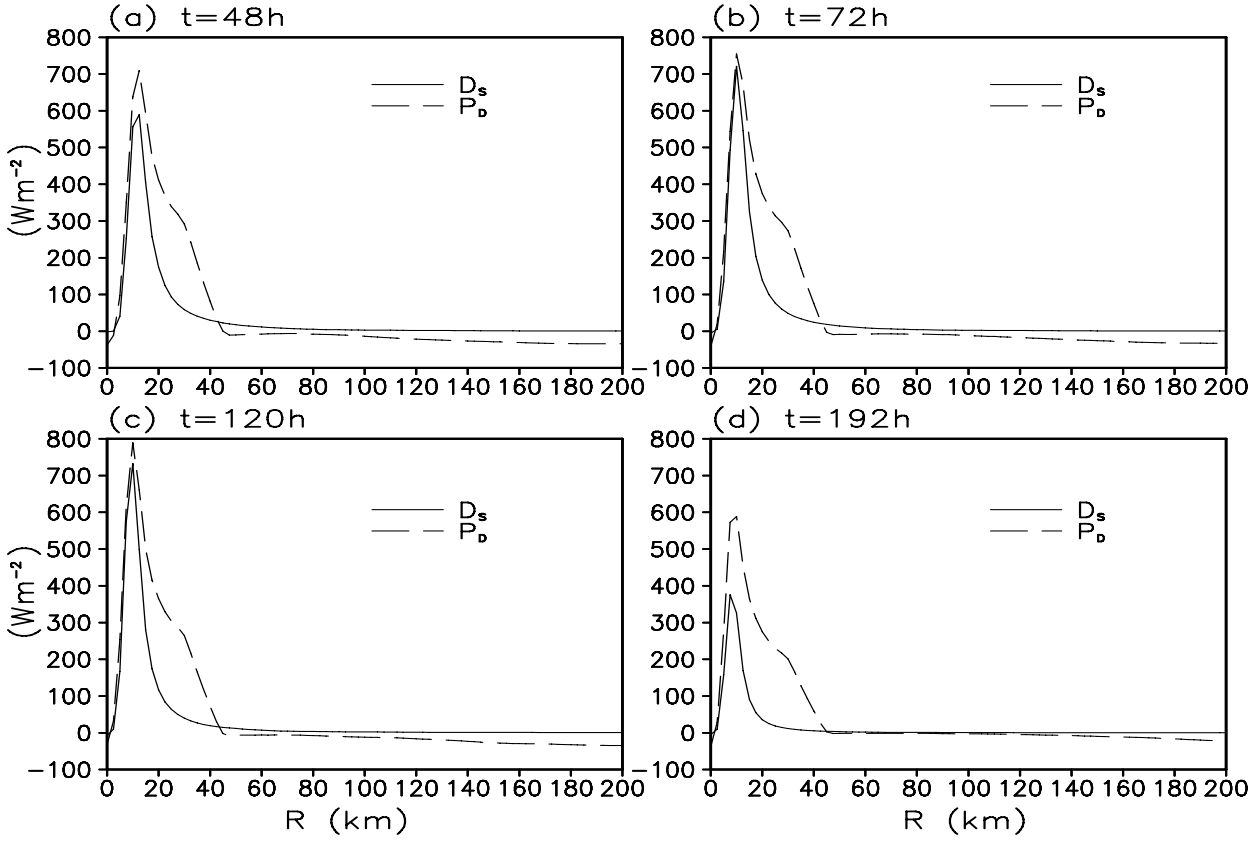

Figure 15. The same as in Fig. 5 but for the sensitivity experiment with the surface entropy fluxes eliminated outside the eyewall. Times shown are after 48 h spin-up in the control experiment.

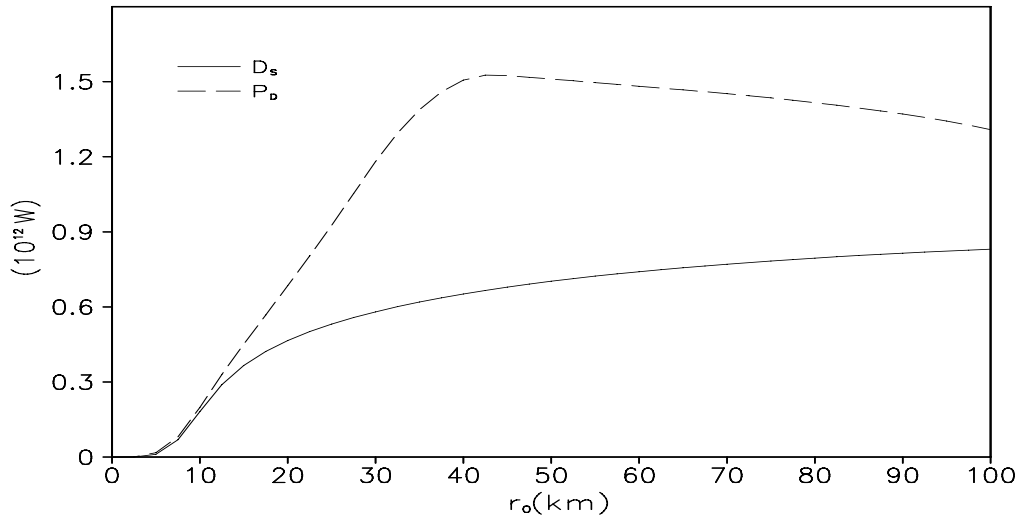

Figure 16. Area-integrated energy production rate (10^{12} W, dashed) and surface frictional dissipation rate (10^{12} W, solid) within a given radius of r_0 after 72 h of simulation in the sensitivity experiment (OE30) with surface entropy fluxes outside the eyewall eliminated.